Electromagnetic Interaction between High Tc Superconductors and Tokamak Plasma

（高温超伝導体とトカマクプラズマとの電磁相互作用）

TETSUYA UCHIKOSHI

内一哲哉

ELECTROMAGNETIC INTERACTION BETWEEN HIGH Tc SUPERCONDUCTORS AND TOKAMAK PLASMAS

（高温超電導体とトカマクプラズマとの電磁相互作用）

TETSUYA UCHIMOTO

B.E., University of Tokyo
(1993)
M.E., University of Tokyo
(1995)

A Dissertation
Submitted to the Department of Quantum Engineering
and Systems Science,
Faculty of Engineering
in Partial Fulfillment of the Requirements
for the Degree of
DOCTOR OF ENGINEERING
at the
UNIVERSITY OF TOKYO

December 1997

Acknowledgments

I would like to acknowledge my supervisor, Professor K. Miya for his continuous guidance, heartfelt encouragement, and prodding throughout this work. I am also thankful for the personal care I received.

I would like to thank Associate Professor Y. Yoshida for valuable discussions in this thesis and valuable help on various occasions. I am also grateful to Assistant Professor K. Demachi for his friendly encouraging assistance.

I am very grateful to Professor R. Albanese, University of Reggio Calabria, Italy for his encouragement of my study and his kind hospitality for about half a year in Italy.

I would also like to acknowledge Mr. Y.Fukuzaki and Mr. T. Yamada for their cooperation in the experiments and the numerical analysis for this thesis. I gratefully acknowledge the valuable discussions with Dr. N. Takeda. Finally, I am grateful the friendship of present and former students in our laboratory.

Contents

1 Introduction 1

1.1 Background and Objectives 1

1.2 Recent Progress and Application of High Tc superconductor 5

1.2.1 Wire and tape 5

1.2.2 Bulk 8

2 Magnetic Interaction between High Tc Superconductors and Plasmas 17

2.1 The Phenomena of Superconductivity 17

2.1.1 Type I and Type II Superconductors 18

2.1.2 Mixed state 18

2.1.3 Flux Flow and Critical Current Density 20

2.1.4 Critical State Model 20

2.1.5 E-J constitutive relation 21

2.2 Plasma Axisymmetric Instability 22

2.2.1 Stabilization using linear normal conductor 25

2.3 Plasma Response to High Tc Superconductor 28

3 Improvement of Plasma Positional Instability with use of HTSC 39

3.1 Introduction 39

3.2 Numerical Formulation 41

3.2.1 Plasma-Conductor Model 41

3.2.2 Shielding Current Analysis in High Tc Superconductors 48
3.3 Verification of Stabilizing effect due to HTSC 49
3.3.1 Configuration 49
3.3.2 Optimization of high Tc superconductors 52
3.3.3 Verification of plasma stabilization due to HTSC 54
3.3.4 Interaction of HTSC coils with poloidal fields during plasma start-up 55
3.4 Technical Issues of HTSC coils 71
3.4.1 Structural support of electromagnetic force of HTSC coils 71
3.4.2 Effect of joint resistivity on stabilizing effect 72
3.4.3 Estimation of nuclear heating 73
3.4.4 AC loss in HTSC coils 75
3.5 Conclusion 84

4 Design of HTSC tokamak **85**
4.1 Introduction 85
4.2 Design procedure and formulae to determine the plasma parameters 86
4.2.1 I-A-B_{tf}-κ analysis methodology 86
4.2.2 Physics and technological model and constraints 87
4.2.3 Design window in I-A-B_{tf}-κ space 90
4.3 Results 91
4.3.1 Determination of plasma parameters 91
4.3.2 Analyses of plasma equilibrium and positional stability 92
4.4 Conclusion 95

5 Reduction of Toroidal Ripple with use of HTSC **103**
5.1 Introduction 103
5.2 Experiment 105
5.2.1 Description of experiment 105

5.2.2 Results 105
5.3 Numerical analysis 106
5.3.1 Formulation 106
5.3.2 Feasibility of Ripple Reduction with use of HTSC 111
5.3.3 Design study 125
5.4 Conclusion 128

6 Conclusions **129**

List of Figures

1.1 Temperature dependence of critical flux density of various high Tc superconductors. 10

1.2 Processing technologies for silver-sheathed oxide superconducting wires (powder-in-tube method). 11

1.3 Critical current density of oxide superconducting films and wires. 12

1.4 Critical current density of Bi-2223 superconducting wires at 4.2 K and 20 K. 12

1.5 Bending strain characteristics of multi-filamenary B-2223 superconducting wire. 13

1.6 Tensile stress tolerance of critical current at 77 K. 13

1.7 Hysteresis loops of magnetization before and after irradiation of 2.4, 4.8, 9.5 and $18 \times 10^2 1/m^2$ in B-2223 superconductors at 60 K. The entire vertical axis corresponds to about 0.13 T for the sample having section of 1.5 mm width and 1 mm thick. 14

1.8 Neutron fluence dependence of critical current $T_c(\bullet)$ and change of c-axis lattice constant $c/c_o(\triangle)$. 14

1.9 Dependence of magnetic field on critical current density for Y-based bulk superconductors at 77 K. 15

1.10 Trapped magnetic flux density distribution in a MPMG processed Y-based bulk superconductors at 77 K. 15

2.1 Magnetization of superconductor 19

2.2 Mix state of type II superconductor 19
2.3 Geometry for calculating plasma positional instability. 22
2.4 System modeled by a point plasma of constant current free to oscillate vertically and a passive conductor. 32
2.5 Supposed input disturbance in the calculation. 32
2.6 Schematic drawing of the plasma response against disturbance and the parameters characterizing the plasma response. 33
2.7 Evolution of the plasma displacement. 34
2.8 Geometry of the superconducting ring and relaxation of the shielding current in the superconducting ring. 35
2.9 Geometry of the superconductor for calculation of hysteresis loss. 36
2.10 Evolution of shielding current in high Tc superconductor. 37
2.11 Evolution of the L/R time of high Tc superconductor. 37
2.12 Plasma in the presence of high Tc superconductors. 38

3.1 schematic drawing of high Tc superconducting plasma stabilizer. 41
3.2 Issues to be discuss in order to realize the plasma stabilization with use of high Tc superconductors. 42
3.3 Schematic drawing of experimental setup. 50
3.4 Electromagnetic force of high Tc superconductor. 50
3.5 Configuration of ITER TAC-8 (EOB) and high Tc superconducting plasma stabilizer. 57
3.6 Ag-sheathed Bi-2223 superconducting tape. 58
3.7 Location of HTSC coils (perfect conductor). 59
3.8 Relation between poloidal location of HTSC coils and its stabilizing effect on plasma. 60

3.9 Relation between size of cross section of HTSC coils and its stabilizing effect on plasma. 60
3.10 Location of HTSC coils. 61
3.11 Relation between location of HTSC coils and its stabilizing effect on plasma. 62
3.12 Relation between size of HTSC coils and its stabilizing effect on plasma. . 62
3.13 Evolution of current density profile in SC2 (5 cm × 5 cm). 63
3.14 Evolution of current density profile in SC2 (30 cm × 30 cm). 64
3.15 Evolution of plasma parameters in case D. 65
3.16 Displacement of reference points at separatrix. 66
3.17 Schematic view of twin loop configuration. 67
3.18 Configuration of connection of twinloop. 68
3.19 Evolution of parameters during plasma start-up. 69
3.20 Effect of twin loop connection on shielding current and stabilization. 70
3.21 Evolution of electromagnetic force acting on high Tc superconductor. . . . 76
3.22 Schematic drawing of SUS316 support for electromagnetic force. 77
3.23 Stress and strain at support structure and high Tc superconducting tape. . 77
3.24 Relationships between resistance of solder joint and joint length at 77 K. . 78
3.25 Effect of joint resistance in HTSC coils on plasma stabilization. 78
3.26 Configuration of neutron transport calculation. 79
3.27 Radial profile of nuclear heating rate in presence of HTSC coils in ITER. . 79
3.28 Relation between temperature rise and nuclear heating. 80
3.29 Experimental setup. 81
3.30 Dependence of temperature rise in high Tc superconductor sample on J-E curve. 82
3.31 Effect of temperature rise on stabilization of plasma. 82
3.32 Radial profile of neutron flux in presence of HTSC coils in ITER. 83
3.33 Evolution of AC loss in SC2 of the HTSC coils 83

4.1 Dependence of aspect ratio and elongation on beta limit. 87
4.2 Schematic drawing of I-A-B phase space. 91
4.3 Geometry of TF coil for calculation. 92
4.4 Decision of operation point in I-A space. 93
4.5 POPCON diagram of HTSC tokamak. 94
4.6 Result of plasma equilibrium analysis. 96
4.7 Configuration of positional stability analysis. 97
4.8 Displacement of plasma centroid in case where high Tc superconducting coils are placed. 98
4.9 Vertical displacement of plasma centroid in case where no high Tc superconducting coil is placed. 98
4.10 Displacement of reference points at separatrix. 99
4.11 Comparison of size between HTSC tokamak and ITER/EDA. 101

5.1 Experimental arrangement. 109
5.2 Relation between magnetic induction and location X at Y = 9 (mm), Z = 0 (mm). 110
5.3 Relation between ripple value and location Y. 110
5.4 Contour lines of ripple magnitude: (a) number of TF coils is 24, (b) number of TF coils is 20. 116
5.5 Two arrangements of superconductors between TF coils. 117
5.6 Arrangement and geometry of superconductor in case 1. 118
5.7 Change of magnetic induction, B_z, in the local coordinate in Fig. * at the center of superconductor in case 1 ($N = 20$). 119
5.8 Ripple value along plasma edge in different access distances. 120
5.9 Relation between flux density, B_z, in the local coordinate in Fig. 5.6 and toroidal angle at the maximum ripple location ($N = 20$). 121

5.10 Contour lines of ripple magnitude in case 1 ($d = 0.5$m). 122
5.11 Arrangement and geometry of superconductor in case 2 d ($N = 20$). 123
5.12 Change of magnetic induction, B_z, in the local coordinate in Fig. 5.11 at the center of superconductor in case 2 ($N = 20$). 124
5.13 Ripple value along plasma edge in different locations ($N = 20$). 124
5.14 Dependence of maximum ripple value in plasma region on width of superconductor assembly (x = 0.2 m, y = 4.0 m, d = 0.4 m). 126
5.15 Critical line for the maximum ripple less than 2.0 % with respect to size in x and y direction. 127

List of Tables

1.1 Main parameters and dimensions of ITER. 4

1.2 High Tc superconductors. 11

3.1 Parameters of ITER/EDA TAC-8 (EOB). 57

3.2 Parameters of HTSC tape. 58

3.3 Location of HTSC coils (perfect conductor) and τ_p in each case. 59

3.4 Location of HTSC coils and τ_p in each case. 61

4.1 Comparison of design parameters between HTSC tokamak and ITER/EDA. 100

Chapter 1

Introduction

1.1 Background and Objectives

The fusion research started over 30 years ago, and since then numerous investigations have been carried out throughout the world, on various kind of reactor types. In the 1970s, the tokamak type reactor started to receive established attention and up to the present it has been the privileged emphasis of fusion research and development efforts. The three big tokamak – JT-60(Japan), JET(EU) and TFTR(US) – which aimed attainment of the break even, started their operation in 1982–1984 and their objectives are almost satisfied. Their main results can be summarized as

1. discharge of high temperature and high density plasma close to break even,
2. success in DT experiment at JET and TFTR,
3. arrangement and provision of database of experimental results.

It follows from the results that an ignition and long-burn can be expected if H-mode is assumed to be achieved with the device of 1000 m^3.

The efficiency of the fusion research and development can be ensured only by following a sequential plan, according to the progress to date. Basically, the goal of realizing the fusion reactor can be attained in three main step: experimental reactor in which the ignition should be achieved, DEMO reactor which demonstrates production of electric power,

and prototype reactor in which economical feasibility is examined. Presently, a large scale international collaboration comprising a frame of four parties – EU, Japan, Russia and United States – is studying the achievability of ignition and long burn of plasmas, which corresponds to the step of experimental reactor. This is the ITER (International Thermonuclear Experimental Reactor) project. The current activity is ITER/EDA (Engineering Design Activity) to continue for 6 years (1992-1998) preceded by the ITER/CDA (Conceptual Design Activity)(1988-1989). Basic parameters of the reactor are listed in Table 1.1.

The ITER design matured from the three milestones – Outline Design Report(Jan. '94) [1], Interim Design Report(Jul. '95) [2] and Detailed Design Report(Dec. '96) [3] – and is evaluated as a comprehensive and consistent design for an experimental fusion reactor. It is supported also by the technical R & D efforts for a large scaled major components, like toroidal field coils, center solenoid coils, vacuum vessel and in-vessel components, like the divertor and blanket modules. All these components are required to show very high performance under very severe operational conditions. Certain types of damages should be accounted for, due to possible abnormal operational conditions like major disruption and vertical displacement events of plasmas. This is why advanced technique for remote maintenance of damaged components is required and now under development. The results already achieved by these R & D activities are impressing. However, there exist some difficulties like high cost and some insufficiency of technology development, which are without doubt caused by the large scale of the machine. They can be ascribed to the change of basic parameters of the reactor from CDA to EDA, in order to secure the long burn and plasma stability. This dilemma embosses the gap between the level of necessary technology to achieve ignition and the current level of fusion technology. Consequently, the introduction of innovative technology is highly required at this point.

One of the promising technologies to be used in fusion reactors is based on high Tc superconductors. The salient features of high Tc superconducting materials are (1)

facility of cooling, i.e. high critical temperature, (2) robustness to instability due to temperature rise, and (3) high critical magnetic field. These features encouraged the research and development of high Tc superconductors and their application is presently considered in many fields of engineering. As for the application of high Tc superconductors to fusion reactors, only the utility of current lead is examined presently [4]. It might not be attractive to apply high Tc superconductors in the frame of magnetic field coils and current leads, where low Tc superconductors are being successfully used. However, the outstanding features of high Tc superconductors make them to be very promising candidates for application where a high level of electromagnetic control is required.

In this study, electromagnetic interaction between high Tc superconductors and tokamak plasmas is examined, with the aim of the further development of fusion reactors, especially introduction of innovative technologies to solve the problems of the current fusion research aforementioned. Based on the results new application of high Tc superconductors to fusion reactors is proposed: (1) improvement of plasma positional instability by using a high Tc superconducting coil, and (2) reduction of toroidal ripple by high Tc superconducting bulks. Feasibility of the application is examined in the configuration of ITER design. In addition, conceptual design is performed, incorporating the application of high Tc superconductors. The effect of high Tc superconductors on fusion plasma performance is analyzed.

Table 1.1: Main parameters and dimensions of ITER.

	EDA	CDA
Total Fusion Power	1.5 GW	1.0 GW
Plasma inductive burn time	1000 sec	400 sec
Plasma current	21 MA	22 MA
Plasma major radius	8.1 m	6.0 m
Plasma minor radius	2.9 m	2.2 m
Elongation	1.6	2.0
Divertor configuration	Single null	Double null
Toroidal field	5.7 T	4.85 T

1.2 Recent Progress and Application of High Tc superconductor

The adjective "high-temperature" is a relative term and generally refers to those new classes of materials that have critical temperatures Tc above 30 K. This class includes the new ceramic materials based on copper and oxygen as well as the fullerene materials based on carbon. Our discussion here will focus mainly on these ceramic superconductors which are listed in Table 1.2 and their upper critical flux densities are shown in Fig. 1.1. As to the advantage of high Tc superconductors, their high critical temperatures are of course cited. It gives us not only facility of cooling due to high operating temperature but also robustness to thermal disturbance owing to high temperature margin and increase of the specific heats of material: for instance, from 4.2K to 20K, by a factor of $\sim$ 100. These properties allow their utilization in the form of bulk, which is impossible for low Tc superconductors because of the flux jump phenomenon [5]. Another salient feature to be mentioned is their high critical flux densities. As is shown in Fig. 1.1, critical flux density of high Tc superconductor at low temperature such as 4.2 K are too high to measure (they are predicted to amount to $\sim$ 100 T) [6–8]. This imply the possibility of application of high Tc superconductor to generation of high magnetic field. On the other hand, the drawbacks of high Tc superconductors are: 1) low critical current density compared with low Tc superconductors and 2) brittleness and mechanical fragility because of ceramic. Here, recent progress of high Tc superconductors are summarized focusing on their outstanding features and drawbacks.

1.2.1 Wire and tape

In applying the high Tc superconducting wire to many engineering field, two points are required: 1) fabrication of long wire and 2) high critical current density. All representative materials such as Bi-based, Y-based and Tl-based superconductors have so called two-dimensionality that the superconducting currents flow along the Cu-O planes which

constitute the a-b planes of the crystal structure called perovskites. This anisotropy of the materials makes fabrication of long wires difficult because Cu-O planes must be oriented along the current path of wires from several hundred meters to several kilometers in length. In addition, critical current density of 10,000 A/cm^2 at least is required in the magnetic field depending on the application: for instance, 0.1 Tesla for power cables, from several Tesla to twenty Tesla for magnet.

In order to achieve the demands, fabrication of high Tc superconducting wire have been attempted using various materials in various method such as the powder-in-tube [9], dip-coat, jerry-roll, CVD(Chemical Vapor Deposition) and laser abrasion method. Wires of Bi-based, Y-based and Tl-based oxides are currently available with the aforementioned methods. Among them, Bi-based wire fabricated by the powder-in-tube method is most promising at present in view of engineering application [10]. Therefore, main properties of silver-sheathed BiSrCaCuO wire wires are introduced in the following.

(a) Development of silver-sheathed BiSrCaCuO wire

There are two superconducting phases in Bi-based high Tc material: 2223 phase with Tc=110 K and 2212 phase with Tc=85 K. Wires of the both phases are available prepared by the powder-in-tube method. However, it is difficult for silver-sheathed Bi-2212 wires to be applied to large coils or power cables, since only the wind-and-react method can be applied in winding Bi-2212 wires. Indeed, large superconducting coils of Nb_3Sn prepared by the wind-and-react method are available, but fabrication of silver-sheathed Bi-2212 wire requires more strict control of temperature accurate to a few degrees in react process. Furthermore, the critical temperature of Bi-2212 phase is 85 K at which enough temperature margin can not be obtained in the case of cooling with liquid nitrogen(77.3 K). Accordingly, we focus on silver-sheathed Bi2223 wire here. The powder-in-tube method is schematically shown in Fig. 1.2. The advantage of the method is that it can fabricate long wires. The reason why silver is used for sheath is that 1) it does not react with

the superconducting material during sintering, 2) it is good for plastic working, and 3) it has small resistivity. To increase flexibility, filament are multiplied. The Cu-O planes of crystals in wires are oriented by rolling mechanically because Bi-2223 phase is easy to cleave. In order to obtain high orientation of grains, it must be rolled to quite thin wire.

(b)Critical current density

The critical current density of silver-sheathed Bi-2223 wire at 77.3K is shown in Fig. 1.3 [11]. Critical current densities of 42,300 A/cm^2 are obtained at external field of 0.1T corresponding application to power cables and 12,000 A/cm^2 at 1T corresponding to application to small coil.

The critical current densities at 4.2K and 20K, which are boiling temperature of liquid helium and hydrogen, respectively, are shown in Fig. 1.4 [12]. Even over 15 T, Bi-2223 wire keeps high critical current density compared with conventional low Tc superconducting wire (NbTi, Nb_3Sn) at 4.2K. In addition, Bi-2223 wire can also be available to high field application even at 20K, which is impossible for conventional low Tc superconducting wire.

(c) Long wire

It is highly required to fabricate long Bi-2223 wire for the application. Recently, over 1000 m class wires are available with the critical current density of 4,020 A/cm^2 at 77.3K. In the case of 100 m long wire, critical current density of 27,800 A/cm^2 at 77.3K is obtained.

(d) Mechanical property

Bi-based superconductors themselves have little flexibility because of the ceramic essence. However, multi-filament structure in silver sheath allows the wire iterative bending after sintering process as is shown in Fig. 1.5 [13]. So as to improve the mechanical property of the wire, addition of Mn and/or Sb to Ag sheath was attempted. Fig. 1.6 shows the

decrease of critical current in applying the tensile stress to wires [10]. In the case of Ag-0.3%Sb/Ag-0.5%Mn sheath, persistence in tensile stress up to 200 MPa was confirmed, which competes with the toughness of Nb_3Sn wires made by the bronze method.

(e) Neutron irradiation

Effect of neutron irradiation is concerned from two viewpoints: 1) estimation of tolerant dose for the fusion application and 2) introduction of effective pinning centers in high magnetic field and at high temperature. From the latter viewpoint, other high energy particles such as electrons, ions, and protons are also effective. Here, effect of neutron irradiation is focused on because of the objective of this study. Fig. 1.7 shows the hysteresis loops of magnetization before and after irradiation in the fluence range from $2.4 \times 10^{21}/m^2$ to $1.8 \times 10^{22}/m^2$ in Bi-2223 at 40 and 60 K. As seen in these figures, the magnetic field penetrates to the center of the sample. Therefore the enhancement of the loop area is considered to be a consequence of the presence of the radiation-induced defects, which corresponds the increase of the critical current density. Up to the fluence of $9.5 \times 10^{21}/m^2$, the increase of loop area was observed. However, after the irradiation of fluence of $1.8 \times 10^{22}/m^2$, loop area decreased. Figure 1.8 shows the neutron fluence dependence of Tc and c-axis lattice constant of Bi-2212 single crystal. It implies that the critical fluence of Bi-based superconductors is of the order of $10^{22}/m^2$.

1.2.2 Bulk

Application in the form of bulk is unique to high Tc superconductors due to their high critical temperatures. Presently, application of bulk superconductors is actively examined in many engineering fields, for instance, magnetic bearing, flywheel for energy storage [16,17], superconducting permanent magnet and so on. The followings can be cited as outstanding features of bulk superconductor; 1) electromagnetic force due to bulk superconductor is mechanically stable, and 2) magnetization of bulk superconductors can be

larger than that of ferromagnetic materials. In the applications of bulk superconductors, three points are required: 1) fabrication of large single crystal bulk, 2) improvement of pinning force, and 3) decrease of weak links. With the current fabrication technologies, only Y-based bulk superconductors prepared by melt-grown processes meet the requirements above. Therefore, main properties of Y-based bulk superconductors are introduced in the followings.

Development of melt-grown processes such as quench-melt-growth(QMG) [18] and melt-powder-melt-growth (MPMG) [19] enables to fabricate Y-based bulk superconductors which possess large pinning force and few weak links. The advantage of the method is that; 1) it can fabricate large size of single crystal bulks, and 2) the pinning centers of Y-211 phase are dispersed uniformly and finely in the sample (Y-211 phase of the smaller grain diameter effectively contributes the pinning). At present, bulks of 0.1 m $\times$ 0.1 m in size are available. Figure 1.9 shows the critical current density for Y-based superconductors. Transport critical current density exceeds $3.0 \times 10^4 A/cm^2$ [20]. Figure 1.10 shows the profile of flux density in a bulk sample measured by a hall probe. The processes of the magnetization are as follows; 1) 3 T of flux density was applied to the sample at room temperature, 2) the sample was immersed and cooled in liquid nitrogen, and 3) applied flux was decreased to 0 T. It should be noted that 1.4 T of flux density was trapped in the sample, which exceeds the residual magnetization of the strongest ferromagnetic materials with the current technologies.

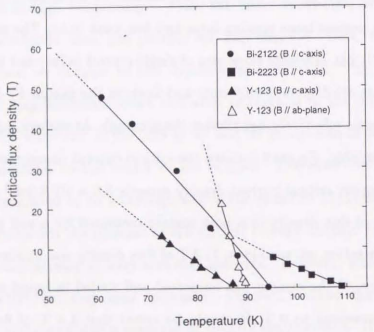

Figure 1.1: Temperature dependence of critical flux density of various high Tc superconductors.

Table 1.2: High Tc superconductors.

Superconductor	T_c (K)
$La_{1.85}\ Ba_{0.15}Cu\ O_4$	35
$La_{1.85}\ Ba_{0.5}Cu\ O_4$	40
$Y\ Ba_2\ Cu_3\ O_7$	95
$Bi_2\ Sr_2\ Ca_1\ Cu_2\ O_8$	85
$Bi_2\ Sr_2\ Ca_2\ Cu_3\ O_8$	110
$Tl_2\ Ba_2\ Ca\ Cu_2\ O_8$	108
$Tl_2\ Ba_2\ Ca_2\ Cu_2\ O_{10}$	125
$Hg\ Ba_2\ Ca_2\ Cu_3\ O_{6+\delta}$	133.5

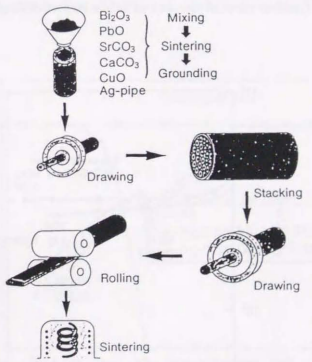

Figure 1.2: Processing technologies for silver-sheathed oxide superconducting wires (powder-in-tube method).

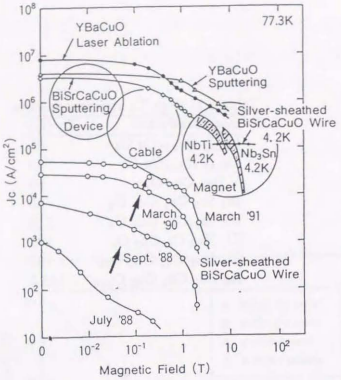

Figure 1.3: Critical current density of oxide superconducting films and wires.

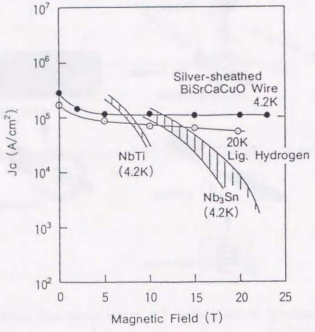

Figure 1.4: Critical current density of Bi-2223 superconducting wires at 4.2 K and 20 K.

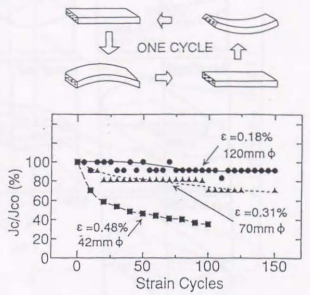

Figure 1.5: Bending strain characteristics of multi-filamenary B-2223 superconducting wire.

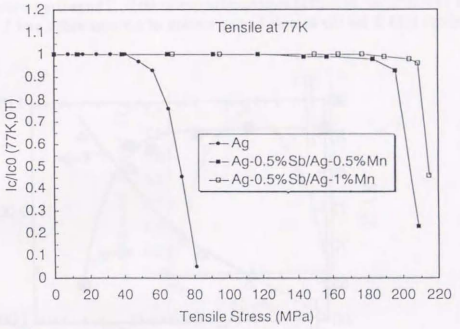

Figure 1.6: Tensile stress tolerance of critical current at 77 K.

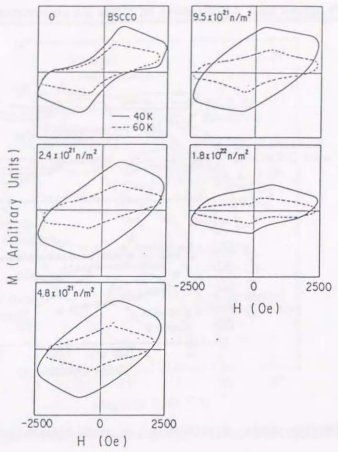

Figure 1.7: Hysteresis loops of magnetization before and after irradiation of 2.4, 4.8, 9.5 and $18 \times 10^2 1/m^2$ in B-2223 superconductors at 60 K. The entire vertical axis corresponds to about 0.13 T for the sample having section of 1.5 mm width and 1 mm thick.

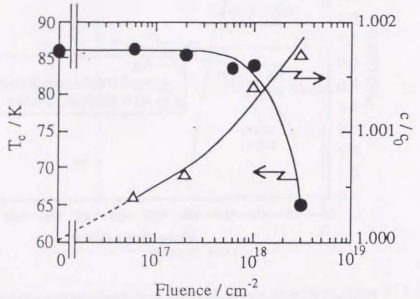

Figure 1.8: Neutron fluence dependence of critical current $T_c(\bullet)$ and change of c-axis lattice constant $c/c_o(\triangle)$.

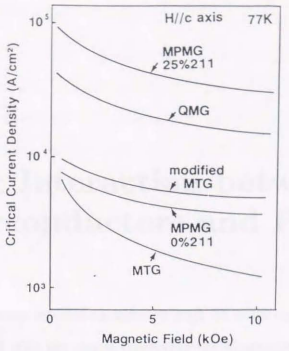

Figure 1.9: Dependence of magnetic field on critical current density for Y-based bulk superconductors at 77 K.

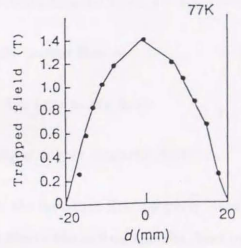

Figure 1.10: Trapped magnetic flux density distribution in a MPMG processed Y-based bulk superconductors at 77 K.

Chapter 2

Magnetic Interaction between High Tc Superconductors and Plasmas

In this chapter, magnetic interaction between high Tc superconductors and plasmas is theoretically discussed with the aim of improving the plasma instability. For the preparation of the discussion, the electromagnetic properties of superconductors and plasmas are outlined at first, which forms a basis for the main discussion of this chapter.

2.1 The Phenomena of Superconductivity

The salient features of superconducting materials are addressed as follows:

- Zero resistance to steady current flow
- Exclusion of magnetic flux lines at low fields
- Flux trapping or pinning at higher magnetic fields

The special stress is laid on the fact that first property, zero resistance, is not due to the perfect conductivity but due to the second and the third properties described above. Therefore, the essence of the phenomena of superconductivity lies in the behavior of magnetic flux lines in their bodies. In the following, the phenomena in superconductors are summarized in view of their magnetic property.

2.1.1 Type I and Type II Superconductors

Superconducting materials are classified as either Type I or Type II due to their magnetic property. Type I materials are often the pure metals and have low values of the critical magnetic field, resulting in low critical current. The magnetization of Type I materials is shown in Fig. 2.1; when the external magnetic field is below the critical magnetic field H_c, they exhibit perfect diamagnetism ,so-called Meissner effect, as

$$M = -H_e. \tag{2.1}$$

On the other hand, Type II materials are generally alloys or compounds, such as Nb-Ti or Nb_3Sn, or the high Tc superconducting oxides such as YBCO or BSSCO, which are able to carry very high current density in high transverse magnetic fields without becoming normal. As is shown in Fig.2.1, there exist two values of the critical magnetic field: the lower critical magnetic field H_{c1} and the upper critical magnetic field H_{c2} At lower magnetic fields than H_{c1}, Type II materials also behave as a Type I material with complete flux exclusion. However, above H_{c1} and below H_{c2} the flux can partially penetrates the material, thereby creating normal and superconducting region. This state is called the mixed state and its microscopic structure is schematically drawn in Fig.2.2. Since there do not exist Type I nor Type II superconducting materials available today which have enough large H_c or H_{c1}, respectively, from the application point of view, application of superconductivity for high field source or magnetic force source can be explained in the frame of the physics of mixed state.

2.1.2 Mixed state

The negative surface energy causes the normal-state, flux-bearing regions to subdivide until a single fluxoid quantum passes through, like a tube, in the otherwise superconducting sample. The tube of flux is called a filament or vortex. This is type II superconductivity, also called the mixed state or vortex state (Fig. 2.2).

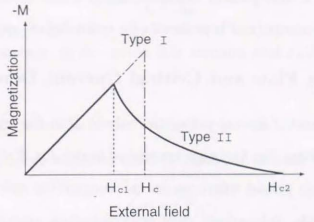

Figure 2.1: Magnetization of superconductor

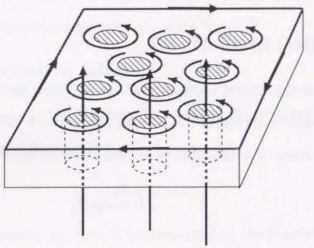

Figure 2.2: Mix state of type II superconductor

In the mixed state, the filament act as tiny bar magnets and repel each other. In the absence of filament pinning centers, the net repulsion energy is minimized when the filaments form a close-packed, hexagonal array, a flux lattice. However, pinning of the filaments often occurs (and is preferable for technological applications).

2.1.3 Flux Flow and Critical Current Density

Consider a current $\boldsymbol{J}$ flowing perpendicularly to $\boldsymbol{B}$ in the mixed state. Then, as a result of the Lorentz force, the filaments are pushed in the $\boldsymbol{J} \times \boldsymbol{B}$ direction. On the other hand, the filaments are pinned where spatial inhomogeneities exist, such as impurities, grain boundaries, voids, dislocations, non-superconducting precipitates, and so on. In other words, the pinning force acts on the filaments against the Lorentz force. As the current increases, the Lorentz force can become of the same order of magnitude as the pinning force. Then the vortices move with a steady motion, their velocity being limited by filament viscous-drag forces. This motion is the flux flow state and it induces an electric field parallel to $\boldsymbol{J}$, which absorbs energy from the circuit and appears as a resistance. The transition current to the flux flow state is called a critical current density, J_c.

2.1.4 Critical State Model

In one theory for the critical transport current advanced by Bean [21], it is assumed that all flux lines move to maximize the pinning force. For a one-dimensional problem, with the transport current $\boldsymbol{J}$ orthogonal to $\boldsymbol{B}$, the following equation is obtained:

$$JB = F_p(B) \tag{2.2}$$

where F_p is the maximum value that a pinning force can attain. This state is called the critical state.

Concerning F_p in eq. (2.2), some models have been proposed. Here, we introduce three models, the Bean model, the Kim model and the Yasukochi model.

1. **Bean model** [21]

   The critical current density $\boldsymbol{J}$ is assumed to have a constant value,

   $$J_c = J_{c0}, \tag{2.3}$$

   where J_{c0} is a constant. In this model it is assumed that $F_p(B)$ is proportional to B.

2. **Kim model** [22]

   Kim et al. proposed an empirical relation, which fits to many experimental results,

   $$J_c = \frac{J'_{c0}}{B + B_0}, \tag{2.4}$$

   where B_0 and J'_{c0} are constants. The equation corresponds to Bean model when $B \ll B_0$. And it means that $F_p = const.$ when $B \gg B_0$.

3. **Yasukochi model** [23]

   In this model, the dependence of J_c on B is expressed as

   $$J_c = \frac{J''_{c0}}{\sqrt{B}}, \tag{2.5}$$

   where J''_{c0} is the critical current density when B = 1 T.

2.1.5 E-J constitutive relation

When the fluxoids moves in the magnetic flux density $\boldsymbol{B}$, with velocity $\boldsymbol{v}$, the following speed electromotive force $\boldsymbol{E}$ is yielded,

$$\boldsymbol{E} = \boldsymbol{B} \times \boldsymbol{v}. \tag{2.6}$$

When the fluxiods moves in the type II superconductor, the kinetic equation is given as

$$\eta_f \boldsymbol{v} = \boldsymbol{J} \times \boldsymbol{B} - \boldsymbol{F}_p, \tag{2.7}$$

where η_f is the viscous coefficient for a fluxoid, $\boldsymbol{J}$ is the shielding current density and $\boldsymbol{F}_p$ is the pinning force. The critical current density J_c is defined as the maximum current

density which does not cause the fluxoids' movement. By substituting $\boldsymbol{v} = \mathbf{o}$ into eq. (2.7), J_c is given as

$$J_c = \frac{F_p}{B}. \tag{2.8}$$

By substituting eq.(2.8) to eq.(2.6), the electric field is obtained as

$$\boldsymbol{E} = \frac{B^2}{\eta_f}(J - J_c) = \rho_f(J - J_c), \tag{2.9}$$

where ρ_f is the flux flow resistivity.

2.2 Plasma Axisymmetric Instability

Elongated tokamak plasmas are susceptible to an axisymmetric instability in which the plasmas undergo a basically vertical motion. Since the eigenmodes have a toroidal dependence $\exp(-in\phi)$ such instabilities are also called $n = 0$ modes. Here, one simple model is introduced and analyzed to illustrate the basic nature of the axisymmetric instability.

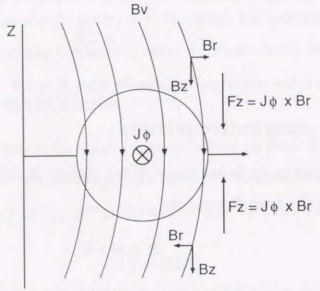

Figure 2.3: Geometry for calculating plasma positional instability.

The calculation treats the plasma as a thin ($a/R_o \ll 1$) current-carrying loop of wire embedded in an externally applied vertical field. For simplicity the effects of plasma

pressure and the internal magnetic flux are neglected. The object of the calculation is to determine the appropriate constraints on the shape of the vertical field to provide stability against rigid vertical and horizontal displacements. Clearly, a pure uniform vertical field $\boldsymbol{B}_v = B_v\boldsymbol{e}_z$, B_v = const., would not be adequate, since by symmetry the system would be only neutrally stable to vertical displacements.

The calculation proceeds by introducing a potential $\phi(R, Z)$, such that the equilibrium forces acting on the plasma are given by $\boldsymbol{F}(R, Z) = -\nabla\phi$. Equilibrium occurs at the point R_o, Z_o where $F_R(R_o, Z_o) = F_Z(R_o, Z_o) = 0$. The condition that the plasma then be stable to a rigid shift in either the vertical or horizontal direction is that $\partial F_Z(R_o, Z_o)/\partial Z_o < 0$ and $\partial F_R(R_o, Z_o)/\partial R_o < 0$ respectively; that is, stability occurs when the restoring force is in the opposite direction of the displacement. Note that because the plasma is a perfect conductor the calculation must be carried out under the constraint that the poloidal flux contained within the current loop be conserved under either plasma displacement.

For the simple model under consideration, the appropriate equilibrium potential and the poloidal flux contained within the current loop are given by

$$\begin{aligned} \phi(R, Z) &= \frac{1}{2}LI^2 \\ \Psi_p(R, Z) &= LI - 2\pi\int_0^R B_Z(R', Z)R'dR' \end{aligned} \tag{2.10}$$

Here, $L(R) = \mu_o R(\ln(8R/a) - 2)$ is the external inductance associated with the toroidal current I and B_Z and B_R are the components of the externally applied vertical field.

The equilibrium forces, calculated from ϕ can be written as

$$\begin{aligned} F_Z &= -LI\frac{\partial I}{\partial Z} \\ F_R &= -LI\frac{\partial I}{\partial R} - \frac{I^2}{2}\frac{L}{R} \end{aligned} \tag{2.11}$$

From ψ = const it hen follows that the equilibrium relation, $\boldsymbol{F}(R_o, Z_o) = 0$ reduces to

$$B_R(R_o, Z_o) = 0$$

$$B_Z(R_o, Z_o) = \frac{I}{4\pi R} - \frac{dL}{dR_o} \tag{2.12}$$

Consider now stability against a rigid vertical shift. Using the fact that $\nabla \times \boldsymbol{B} = 0$ for the externally applied vertical field one can easily calculate $\partial F_Z(R_o, Z_o)/\partial Z_o$. One finds

$$\frac{\partial F_Z}{\partial Z_o} = -\frac{I^2}{2R_o}\frac{dL}{dR_o}n, \tag{2.13}$$

where

$$n(R_o, R_o) = -\left(\frac{R}{B_Z}\frac{\partial B_Z}{\partial R}\right)_{R_o, Z_o} \tag{2.14}$$

is known as the decay index. The condition for vertical stability is thus given by

$$n > 0 \tag{2.15}$$

This condition can easily be understood from Fig. 2.3. If the directions of the vertical field and toroidal current are shown then (1) the vertical field produces an inward force for toroidal equilibrium and (2) a small upward shift of the plasma gives rise to a downward $\boldsymbol{J} \times \boldsymbol{B}$ of magnitude $2\pi RIB_R$, which is in the direction to restore equilibrium. Thus, the curvature of vertical field shown in Fig. 2.3 is the appropriate one for stability, and corresponds to the condition $n > 0$.

In general, for circular-cross-section plasmas axisymmetric stability is relatively easy to achieve, requiring only a modest shaping of the vertical fields. The situation is more serious for elongated tokamaks. In such configurations there is a strong tendency for the plasma to be unstable to vertical shifts as the elongation increases. A number of calculations which derive a more accurate form of the vertical stability condition and relate the elongation b/a to n indicate that only rather small elongations, $b/a < 1.25$, can be stable to vertical shifts when no conducting wall is present. Also, with no wall the critical elongation does not depend very strongly on β_p or the current profile. If a conducting wall is allowed even a moderate distance away, $a_{\text{wall}}/a_{\text{plasma}} \sim 1.5-2.0$ there is

a substantial improvement in vertical stability. However, the necessity of such a wall in a reactor is a disadvantage. Even more important, such a wall would certainly be resistive on the reactor time scale, implying the requirement of a feedback system for vertical positioning. This would be in addition to the horizontal feedback system required for metering the plasma column along the major radius. It is currently thought that through a combination of careful design and modest active or passive feedback, elongations on the order of $\kappa = 1.6 - 2.0$ should be readily attainable in actual experiments.

2.2.1 Stabilization using linear normal conductor

The $n = 0$ axisymmetric modes occur on the poloidal Alfvén time scale,

$$\gamma \sim \left(B_p^2/\mu_o\rho_o\right)^{1/2}\frac{1}{a} \tag{2.16}$$

which is of the order of $(\mu s)^{-1}$ for typical tokamak parameters. Passive conductors such as shaping coils and the vacuum vessel walls stabilize the $n = 0$ axisymmetric modes through the formation of eddy currents. However, these stabilizing eddy currents decay on the order of the L/R time of the passive conductors, leaving the plasma unstable on this slower time scale ($\sim$ 100 ms). To stabilize the plasma on this slow time scale, an active feedback system is usually required. Here, plasma responses in the presence of normal conductors are estimated by reducing complicated tokamak systems to an simple model consisting of point plasma and a passive conductor as is shown in Fig. 2.4. The circuit equation for a single passive coil can be written

$$L_c\frac{dI}{dt} + r_cI + M'_{cp}\frac{\partial Z}{\partial t} = 0. \tag{2.17}$$

Here L_c is the self inductance of the coil which carries the current I and has the resistance r_c. $M_{cp}(Z)$ is the mutual inductance between the coil and the plasma and primes denote derivatives with respect to Z. The plasma undergoes a force due to the external field gradient and the eddy currents. Thus, its equation of motion is

$$m\frac{\partial^2 Z}{\partial t^2} = I_pM'_{cp}I + I_p2\pi R\frac{\partial B_r}{\partial Z}Z. \tag{2.18}$$

Here, the plasma is represented as a wire loop of mass m carrying a constant current I_p, and having a fixed radius R but free to oscillate vertically. Combining eqs.(2.17) and (2.18), the system equation is derived as

$$m\left\{\frac{\partial^3}{\partial t^3}z+\gamma_r\frac{\partial^2}{\partial t^2}z+(\omega_1^2-\omega_o^2)\frac{\partial}{\partial t}z-\omega_o^2\gamma_r z\right\}=0. \tag{2.19}$$

where $\gamma_r = r_c/L_c$ is the inductive resistive decay rate, $\omega_0^2 = (I_p/m)2\pi R\partial B_r/\partial Z$ is the unstable growth rate, and $\omega_1^2 = I_p^2 M_{cp}'^2/mL_c$ represents the stabilizing effect of the passive coil. The proper equation of eq.(2.19) has three roots (to lowest order in $\gamma_r^2/\omega_o^2 \ll 1$);

$$\gamma_1 = \gamma_r\omega_o^2/(\omega_1^2-\omega_0^2) \tag{2.20}$$

$$\gamma_{2,3} = \pm i\left[\omega_1^2-\omega_0^2\right]^{1/2}-\frac{\gamma_r}{2}\frac{\omega_1^2}{\omega_1^2-\omega_0^2}. \tag{2.21}$$

If the passive term is large enough, i.e. $\omega_1^2 > \omega_0^2$, then the system is neutrally stable on the fast time scale. The introduction of the coil resistance is seen to damp the oscillatory modes (2 and 3). However, mode 1, which has zero growth rate in the absence of resistivity, is now unstable. This mode corresponds to a new equilibrium point moving away from $Z = 0$ on the slow time scale.

To investigate transient response of plasma to passive coils, the transfer function of the system is considered. Here, input is chosen as the external force acting on the plasma and output is vertical displacement of the plasma. After the Laplace transform of eqs. (2.17) and (2.18), the transfer function of the system is derived as

$$G(s) = \frac{s+\gamma_r}{m(s^3+\gamma_r s^2+(\omega_1^2-\omega_0^2)s-\omega_0^2\gamma_r)} \tag{2.22}$$

Possible disturbances are minor disruptions, sawtooth oscillations, quick changes of the external field, etc.. To simulate these disturbances, input shown in Fig. 2.5 is considered, which is quick change over a few milli-second followed by a plateau. It is similar to the step function, which is expressed as a simple form of $R(s) = 1/s$ after the Laplace transform. However, the step function is not a proper approximation since actual change

of disturbances are longer compared with the fast time scale of plasma response ω_o. The Laplace transform of the input shown as Fig. 2.5 is

$$R(s) = \frac{f_o}{t_d s^2}\left\{1-\exp(-t_d s)\right\} \tag{2.23}$$

Plasma response to the input is

$$\begin{aligned} Z(t) &= \mathcal{L}^{-1}G(s)R(s) \\ &= F(t) \qquad (0<t<t_d) \\ &= F(t)-F(t-t_d) \qquad (t_d<t) \end{aligned} \tag{2.24}$$

where

$$F(t) = \frac{f_0}{t_d m}\left\{K_0+K_1 t+K_2\exp(\gamma_1 t)+K_3\exp(\gamma_2 t)+K_4\exp(\gamma_3 t)\right\} \tag{2.25}$$

$$\begin{aligned} K_0 &= -\frac{\omega_1^2}{\omega_o^4\gamma_r} \\ K_1 &= -\frac{1}{\omega_o^2} \\ K_2 &= \frac{\gamma_1+\gamma_r}{\gamma_1^2(\gamma_1-\gamma_2)(\gamma_1-\gamma_3)} \sim -K_0 \\ K_3 &= \frac{\gamma_2+\gamma_r}{\gamma_2^2(\gamma_2-\gamma_1)(\gamma_2-\gamma_3)} \\ K_4 &= \frac{\gamma_3+\gamma_r}{\gamma_3^2(\gamma_3-\gamma_1)(\gamma_3-\gamma_2)} = \bar{K}_3. \end{aligned}$$

The parameters characterizing the plasma response are schematically shown in Fig. 2.6: offset s_1, overshoot s_2 and time constant of oscillatory damping on the fast time scale T_o and instability on the slow time scale T_i. They are approximately expressed as

$$\begin{aligned} &s_1 = K_1 t_d + K_0\exp(\gamma_1 t_d) \\ &0 < s_2 < 4|K_3|\exp\left\{Re(\gamma_{2,3})t_d\right\} \\ &T_o = Re(\gamma_{2,3}) \\ &T_i = \gamma_1 \end{aligned} \tag{2.26}$$

The transient response of the plasma of $m = 1 \times 10^{-3}$(kg), $I_p = 20$(MA), $R = 8.0$(m), in the presence of passive coil of $R_c = 9$(m), $Z_c = 2.5$(m), γ_r=1.9(1/s) is estimated applying the disturbance of f_o=1.0 $\times 10^6$ (N), $t_d = 1.0$(ms). The evolution of plasma displacement is shown in Figs. 2.7. It can be recognized that plasma response has two time scale: the Alfvén time and the L/R time of superconductors. In the shorter time scale plasma is stable but in the other time scale it is not stable.

2.3 Plasma Response to High Tc Superconductor

Since electromagnetic property of high Tc superconductor is non-linear as is discussed in section 2.1, the plasma response to high Tc superconductor can not be easily calculated. In addition, the plasma response will vary due to the difference of inputs because of the non-linearity. Thus, plasma response is evaluated here adopting a representative input disturbance and making some assumptions. Here, we consider the same configuration as in Fig. 2.4 except that the passive coil is a high Tc superconductor instead of a normal conductor. The reference disturbance is also the same as is shown in Fig. 2.5. The time domain is divided into two regions: the rapid change region ($0 < t < t_d$) and the plateau region ($t_d < t$). The behavior of the shielding current in high Tc superconducting ring in the two regions are separately taken into account as follows.

(1) rapid change region

Since large electric field is induced in high Tc superconducting ring due to the quick displacement of the plasma as seen in the previous section, the shielding current flows based on the flux flow phenomena. Skin depth $\delta(=\sqrt{1/\omega\sigma\mu})$ of shielding current is the order of millimeter in the case where the disturbance of f_o=1.0 $\times 10^6$ (N), $t_d = 1.0$(ms) is applied in the configuration from Fig. 2.4, and is negligible compared with the minor radius of the superconducting ring. Therefore, in the rapid change region the shielding current flows only at the surface of ring with flux flow resistivity.

(2) plateau region

The surface current induced at the rapid change region decays into broader current flowing at critical current density J_c. In order to calculate the time scale of the relaxation, the following assumptions are introduced;

1. Surface current decays owing to the flux flow phenomenon.

2. Permeation of current into the body of high Tc superconducting ring proceeds based on the critical state model, i.e. the volumetric current flows at critical current density invariably and everywhere.

Consider the geometry of the high Tc superconducting ring as is shown in Fig. 2.8. The calculation treats the superconducting ring as a thin ($a/R \ll 1$) loop of circular cross-section, thus, distributions of current and magnetic field are supposed to be uniform in the radial direction. The relaxation of shielding current in the high Tc superconductor is schematically displayed in Fig. 2.8. The high Tc superconducting ring is divided into two region: surface region and volumetric region. Circuit equation for each region can be written

$$\text{surface region:} \quad L_1\frac{dI_1}{dt} + M_{12}\frac{dI_2}{dt} + R_f(I_1 - I_{C1}) = 0, \tag{2.27}$$

$$\text{volumetric region:} \quad L_2\frac{dI_2}{dt} + M_{12}\frac{dI_1}{dt} + R_{HYS}I_2 = 0. \tag{2.28}$$

Here, L_1 and L_2 are the self inductances of the surface region and the volumetric region, respectively, M_{12} is the mutual inductance between the two regions, R_f is the flux flow resistance, I_{C1} is the critical current of surface region and R_{HYS} is the resistance which is consistent with the hysteresis loss. The external inductance L_{ex} of the ring is

$$L_{ex} = \mu_o R\left[\ln(8R/a) - 2\right]. \tag{2.29}$$

When the current flows in the region of $a < r < b$ (see Fig.2.9), the internal inductance L_{in} of the ring is

$$L_{in} = \mu_o R \frac{1}{(b^2-a^2)^2}\left[\frac{b^4-a^4}{4} - a^2(b^2-a^2) + a^4 \ln\frac{b}{a}\right]. \tag{2.30}$$

Thus, L_1, L_2 and M_{12} are expressed as

$$\begin{aligned} L_1 &= M_{12} = L_{ex}, \\ L_2 &= L_{ex} + L_{in}, \end{aligned} \tag{2.31}$$

Derivation of R_{HYS} is slightly complicated. At first, hysteresis loss W was calculated based on the following assumptions: (1) dependence of J_c on the magnetic field is not taken into account, i.e. the Bean model is applied, (2) the ring is supposed to be straight because $R \ll a$. Consider the configuration shown in Fig. 2.9, which is modeled based on the above assumptions. When the volumetric current flows in the region of $a < r < b$, radial component of the magnetic flux density $B_\theta(r)$ and longitudinal component of the electric field E_z are

$$B_\theta(r) = \frac{\mu_o J_c (r^2-a^2)}{2r}, \tag{2.32}$$

and

$$\begin{aligned} E_z(r) &= \frac{\partial}{\partial t}\left\{\int_a^r B(r)dr\right\} \\ &= -\frac{\mu_o J_c}{2}\frac{\partial}{\partial t}\left\{\frac{r^2-a^2}{2} - a^2\ln\frac{r}{a}\right\}. \end{aligned} \tag{2.33}$$

Poynting vector at the surface of the ring can be written

$$\begin{aligned} \boldsymbol{S} &= \frac{1}{\mu_o}\boldsymbol{E}\times\boldsymbol{B} = -\frac{1}{\mu_o}E_z(b)B_\theta(b) \\ &= \frac{\mu_o I}{4\pi b}\frac{\partial}{\partial t}\left\{\frac{I}{2\pi} + \left(b^2 - \frac{I}{\pi J_c}J_c \ln\sqrt{1-\frac{I}{\pi b^2 J_c}}\right)\right\}. \end{aligned} \tag{2.34}$$

Therefore, hysteresis loss per unit volume P is

$$P = -S\frac{4\pi^2 bR}{2\pi^2 b^2 R} - \frac{1}{2\pi^2 b^2 R}\frac{\partial W}{\partial t}, \tag{2.35}$$

where W is the magnetic energy. Since R_{HYS} is related to the hysteresis loss as

$$R_{HYS} I^2 = P \cdot 2\pi^2 b^2 R, \tag{2.36}$$

R_{HYS} can be written

$$R_{HYS} = -\frac{\mu_o R}{I}\frac{\partial}{\partial t}\left\{\frac{I}{2\pi} + \left(b^2 - \frac{I}{\pi J_c}J_c\ln\sqrt{1-\frac{I}{\pi b^2 J_c}}\right)\right\} - \frac{1}{2}L_2\frac{dI}{dt}\frac{1}{I}. \tag{2.37}$$

The preparation for estimating plasma response to superconductors is completed in the above.

Implementation of calculation

The circuit equations introduced above are numerically solved in the configuration shown in Fig. 2.4 and parameters are the same as in the previous section. The critical current density and flow resistivity of superconductor ring is 1.0×10^7 A/m^2 and 1.0×10^{-9} Ωm, respectively. Relaxation of the currents in two region is displayed in Fig.2.10. The surface current decays to the critical current. Here, the L/R time of the system is defined as

$$\tau_s = 2\frac{W}{P_{joule}} = \frac{\{I\}^T[L]\{I\}}{\{I\}^T[R]\{I\}} \tag{2.38}$$

where P_{joule} is the joule loss. The evolution of τ_s is shown in Fig. 2.11. τ_s increases with the relaxation of shielding current in high Tc superconductor, while τ_s for normal conductors does not change temporally. Just after the disturbance, τ_s is small, which is expected to contribute to the damp of plasma oscillation. On the other hand, after the relaxation is proceed, τ_s gets large enough compared with the L/R time of normal conductor and the period of plasma discharge, plasma instability does not grow. Using $\tau_s (= 1/\gamma_r)$ obtained in the present calculation, plasma response is estimated based on eq.(2.25). From the figure it can be concluded that high Tc superconductor stabilize plasma in both time scale of the Alfvén time and the L/R time of superconductors. This knowledge is bound up with the attractive application of high Tc superconductors, which is described in the next chapter.

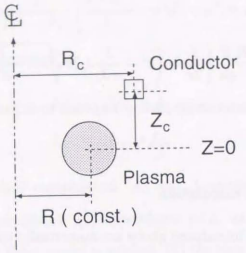

Figure 2.4: System modeled by a point plasma of constant current free to oscillate vertically and a passive conductor.

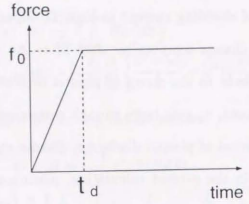

Figure 2.5: Supposed input disturbance in the calculation.

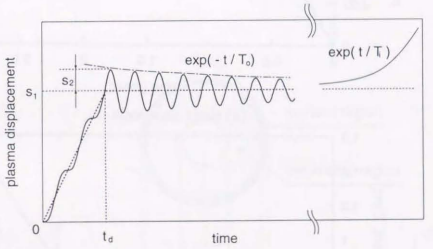

Figure 2.6: Schematic drawing of the plasma response against disturbance and the parameters characterizing the plasma response.

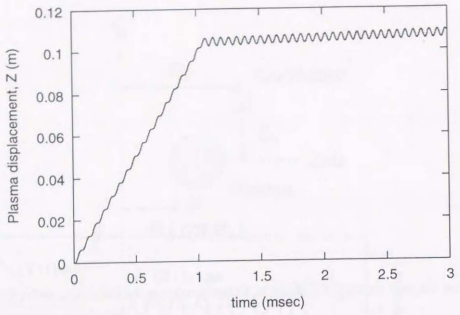

(a) short time scale

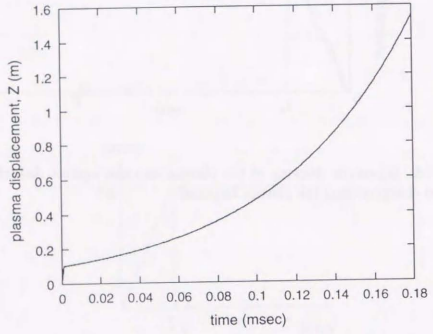

(b) long time scale

Figure 2.7: Evolution of the plasma displacement.

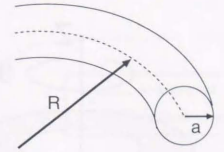

(a) Configuration of supercnoducting ring

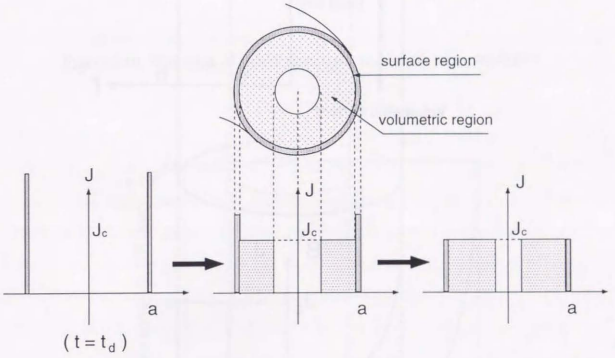

(b) Relaxation of shielding current in superconducting ring

Figure 2.8: Geometry of the superconducting ring and relaxation of the shielding current in the superconducting ring.

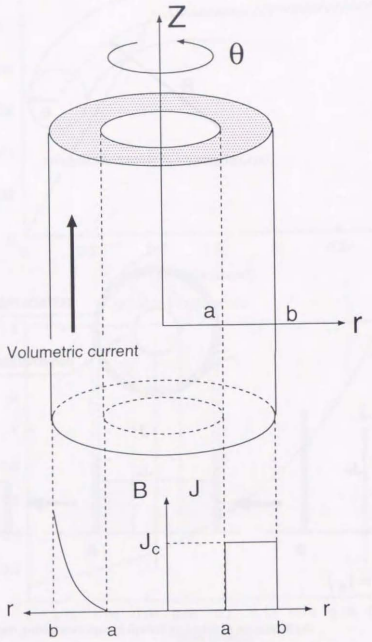

Figure 2.9: Geometry of the superconductor for calculation of hysteresis loss.

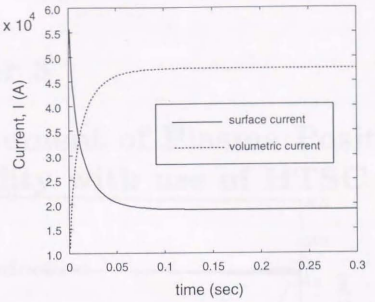

Figure 2.10: Evolution of shielding current in high Tc superconductor.

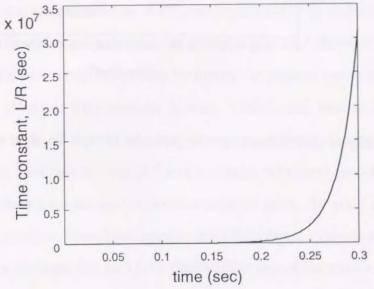

Figure 2.11: Evolution of the L/R time of high Tc superconductor.

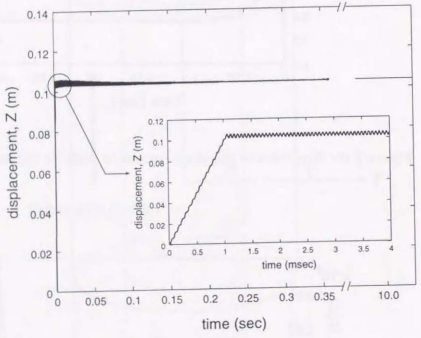

Figure 2.12: Plasma in the presence of high Tc superconductors.

Chapter 3

Improvement of Plasma Positional Instability with use of HTSC

3.1 Introduction

Vertical elongations of plasma cross sections in tokamak fusion reactors are of great advantage to achieve high β values [24], which will lead to compact reactors. Such large elongations, however, make the plasma susceptible to an axisymmetric MHD positional instability in the vertical direction [25, 26]. This positional instability is usually reduced by feedback control system consisting of PF coils supported with stabilizing eddy current induced in the surrounding structure of the plasmas [26, 28]. However, if the feedback control system fails to control the plasma position, the plasma moves drastically in the vertical direction (Vertical Displacement Events, VDEs), and touches a first wall or a divertor, resulting in huge amount of poloidal current in those structures [29–31]. The induced current is called halo current [32] and it couples with large toroidal magnetic field and generates an enormous amount of electromagnetic force. In addition, several types of damages are caused by large heat impact from the plasmas into the components. It follows from severe damages due to VDEs that VDE is one of the most critical issues and innovative method to reduce it is required in the design activity of ITER.

As is examined in chapter 2, high Tc superconductors (HTSC) have the ability to improve the plasma positional instability when they are installed in the plasma periphery.

The stability of tokamak plasmas is attained by the shielding current – which is induced to keep constant magnetic flux penetrating the high Tc superconductor loop – suppressing motion of a current carrying plasma column as shown in Fig. 3.1. This stabilizing system has significant advantages compared with the conventional stabilizers stated as follows;

1. It requires no power supply unlike conventional feedback control systems.
2. Its stabilizing effect on plasmas is free of decay with time which is observed in that of eddy current induced in conducting structures.
3. It is free from quench for different from low Tc superconductors.

In this section, stabilization method of plasmas due to the high Tc superconductor is proposed and its effects are investigated. Many issues are to be addressed in order to realize the stabilization of the plasmas with use of high Tc superconductors and they are summarized in a form of a flow chart in Fig. 3.2.

First of all, coupling analysis between plasma equilibrium and shielding current in HTSC should be mentioned as is discussed in detail in the next section. The coupling analysis conducted here is particular in the sense that it deals with not only eddy current in the normal conductor but also shielding current in superconductors which is characterized by the behavior of fluxoid, as is mentioned in chapter 2. In addition, it is required to incorporate recent knowledge on various properties of the critical current density, which have been actively investigated, to the shielding current analysis.

The second issue to be examined is a consistency with the plasma operation. Particularly, problem of plasma start-up is cited; magnetic flux provided for the plasma by Center Solenoid (CS) coil and several Poloidal Field (PF) coils may be consumed in part by the high Tc superconducting coils. This problem is discussed in the later section.

Finally, the applicability of high Tc superconductor to fusion environment must be examined. In applying the high Tc superconductors to an actual fusion device, they are subjected to severe environment of a fusion reactor: neutron irradiation, nuclear

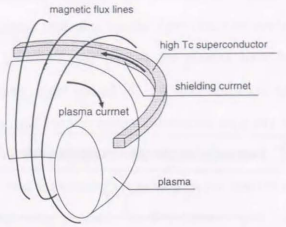

Figure 3.1: schematic drawing of high Tc superconducting plasma stabilizer.

heating, electromagnetic force, etc.. Therefore, shielding against the neutron irradiation and structural support against the electromagnetic force are to be designed.

3.2 Numerical Formulation

In this study, evaluated is the plasma response to possible disturbances in the presence of high Tc superconductors. In this case, two concerns are exist: proper choice of a plasma model and accurate evaluation of shielding current in high Tc superconductors. In this section, answers to the concerns are described.

3.2.1 Plasma-Conductor Model

Comparison of plasma-conductor models

There are various models which take into account the eddy current and plasma equilibrium constraints. Among those, we first mention the full MHD model including transport and diffusion that are treated basically in the nonlinear tokamak simulation code TSC [33]. A real problem of this code is to invert an elliptic operator each time step using a dynamic relaxation method that can lead to errors if the iteration tolerance is too large and can be time consuming if it is too small.

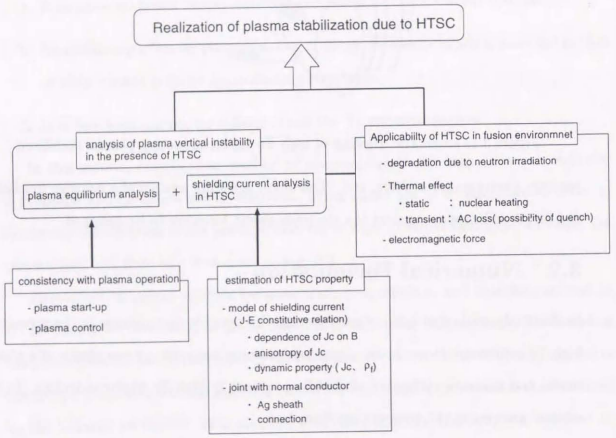

Nomenclature: SC: superconductor
HTSC: high Tc superconductor
J_c: critical current density
ρ_f: flux flow resistivity

Figure 3.2: Issues to be discuss in order to realize the plasma stabilization with use of high Tc superconductors.

In the case where plasma displacement is small and effect of boundary plasma is negligible, linearized plasma response model describes the evolution of various plasma parameters efficiently. Several linear models for plasma have been devised, which are categorized into two types: rigid model [35, 34] and non-rigid one [36, 37]. The former represents the plasma as rigid current source (and often an array of axisymmetric current-carrying filaments) free to move rigidly in the vertical direction. This approach to vertical stability analysis has several drawbacks, all related to the inaccuracy of the plasma model. In particular, it fails to account properly for flux conservation, and it can not in general simulate the correct energy-minimizing approximate plasma responses to coil and vacuum vessel current perturbations. Another category of linear models is the modified inductance method which uses equilibrium perturbation to determine the plasma response to toroidal currents. This approach assumes that the plasma is always in an equilibrium and its equilibrium is expressed as a linear combination of the set of perturbed equilibria. This assumption is derived from the fact that plasma mass is negligible. As is discussed in chapter 2, the momentum equation of the plasma in the presence of a conductive shell has two time scales: the Alfvén time of the plasma and the L/R time of the shell. Usually, the first is much shorter than the second so that the inertia term in the momentum equation can be neglected appropriately if we pay attention to the phenomena whose time scale is longer than the L/R time of the shell. The modified inductance method suppresses the rigid model in the sense that it is MHD consistent and deformable plasma can be treated as simply as a rigid model.

In this study, stabilizing effect of high Tc superconductors on plasmas is investigated, so that behaviors of stabilized plasmas is exclusively of interest. In this situation, it is required to compute the plasma response accurately and efficiently in the case where change of plasma parameters is small. In the sense, the modified inductance method meets the requirement of this study.

Modified inductance method

Since the plasma is supposed to be in equilibrium at each time due to the massless approximation, conductors determine how it moves from one equilibrium to the next. In this study, conducting structures that provide significant toroidal current paths are represented by an array of discrete conducting loops. Changes in the poloidal beta, β_p and an internal inductance, l_i are treated as external disturbances, so that plasma current profile is prescribed during the evolution. In this case, changes of flux functions at the conductors are described as follows linearizing around a plasma equilibrium of interest:

$$\boldsymbol{\Phi} = 2\pi\boldsymbol{\psi} = \boldsymbol{L}^{*}\delta\boldsymbol{I} + \boldsymbol{C}\delta\boldsymbol{d}, \tag{3.1}$$

where $\boldsymbol{\Phi}$ is the set of the poloidal flux, $\boldsymbol{\psi}$ is the set of the flux functions, $\boldsymbol{I}$ is the set of the currents flowing in the conductors, $\boldsymbol{d}$ is the set of the prescribed disturbances, and components of matrices L^{*} and C are

$$\begin{aligned} L^{*}_{ij} &= 2\pi\frac{\partial\psi_j}{\partial I_i} = 2\pi\frac{\Delta\psi_j}{\Delta I_i}, \\ C_{ik} &= 2\pi\frac{\partial\psi_j}{\partial d_k} = 2\pi\frac{\Delta\psi_j}{\Delta d_k}. \end{aligned}$$

A set of currents in the conductors is governed by circuit equations that describe the evolution of the poloidal flux at the locations of the conductors:

$$\dot{\boldsymbol{\Phi}} + \boldsymbol{R}\boldsymbol{I} = \boldsymbol{V}, \tag{3.2}$$

where $\boldsymbol{R}$ is the diagonal resistance matrix for the conductors and $\boldsymbol{V}$ the set of external voltages applied to the conductors. Consequently, the evolution of currents in the conductors in the presence of the plasma is described as: combining Eqs. (3.1) and (3.2):

$$\boldsymbol{L}^{*}\delta\boldsymbol{I} + \boldsymbol{R}\delta\boldsymbol{I} + \boldsymbol{C}\delta\boldsymbol{d} = \boldsymbol{V}. \tag{3.3}$$

Using the set of the currents determined by the above equation, expressed is the output equation which describes the plasma parameters of interest such as positions of reference points at the separatrix, the plasma current and the plasma centroid;

$$\boldsymbol{Y} = \boldsymbol{A}\delta\boldsymbol{I} + \boldsymbol{B}\delta\boldsymbol{d} \tag{3.4}$$

where $\boldsymbol{Y}$ is the set of the plasma parameters of interest and matrices $\boldsymbol{A}$ and $\boldsymbol{B}$ are

$$\begin{aligned} A^{*}_{ij} &= \frac{\partial Y_j}{\partial I_i} = \frac{\Delta Y_j}{\Delta I_i}, \\ B_{ik} &= \frac{\partial Y_j}{\partial d_k} = \frac{\Delta Y_j}{\Delta d_k}. \end{aligned}$$

In this study, we evaluated matrices $\boldsymbol{L}^{*}$, $\boldsymbol{C}$, $\boldsymbol{A}$ and $\boldsymbol{B}$ in the state and output equations (3.2) and (3.4) with use of the well established code TOFU of Japan Atomic Energy Research Institute [38], which compute the motion of separatrix satisfying equation of motion assuming linear deformation of plasma. As for the data of the base equilibrium, this code employs outputs of the plasma equilibrium code SYSTEQ [40] which was also established in Japan Atomic Energy Research Institute. Perturbing the currents, the internal inductance and the poloidal beta of the base equilibrium, TOFU code estimates new equilibria based on the same calculation method as SYSTEQ code, which is described in detail later. Then, it evaluates each components of the matrices which is expressed as incremental ratio shown as Eqs. (3.2) and (3.4). Here, plasma current profile is supposed to be unchanged during the evolution.

Plasma Equilibrium

Equilibrium of the plasma of interest is solved with use of a descendant of the free-boundary MHD equilibrium code EQUCIR [39], called SYSTEQ [40]. Here, described are the details of the formulation and the numerical procedure of SYSTEQ which are also employed in TOFU code in obtaining the set of perturbed equilibria. The axisymmetric MHD equilibrium of a plasma is described by the Grad-Shafranov equation,

$$\nabla^{*}\psi = \mu_o r j_\phi(\psi) = -\mu_o r^2 p' - f f', \tag{3.5}$$

where

$$\nabla^* \psi = \frac{\partial^2 \psi}{\partial r^2} - \frac{1}{r}\frac{\partial \psi}{\partial r} + \frac{\partial^2 \psi}{\partial} z^2, \tag{3.6}$$

and p is the pressure function and f is the toroidal field function. The physical boundary conditions are that the poloidal flux vanishes on the toroidal axis and at infinity, i.e.,

$$\psi(0, z) = 0, \tag{3.7}$$

$$\lim_{r \to +\infty} \psi(r, z) = 0, \tag{3.8}$$

$$\lim_{z \to +\infty} \psi(r, z) = 0, \tag{3.9}$$

In addition, following two constraints are imposed on the plasma;

$$j_\phi = \begin{cases} c j_\phi^* & \text{for} \psi \geq \psi_s \\ 0 & \text{for} \psi < \psi_s \end{cases} \tag{3.10}$$

$$I_p = \int_{\text{plasma}} j_\phi ds, \tag{3.11}$$

where ψ_s is the flux function at plasma surface, the function j_ϕ^* is a specified current density profile and the c is a factor to be adjusted to maintain the plasma current I_p.

SYSTEQ code solves the Grad-Shafranov equation in the form of the integral equation with the Green's function $G(r, z; r', z')$:

$$\psi_p = \int \int_{\text{plasma}} dr' dz' G(r, z; r', z') j_\phi(\psi_p + \psi_c, r', z'), \tag{3.12}$$

$$\psi_c = \sum_k I_k G(r, z; r', z'), \tag{3.13}$$

where ψ_p and ψ_c is the contribution from the plasma current and the coil currents, respectively. The Green's function is given by

$$G(r, z; r', z') = \frac{\mu_o}{\pi \kappa} \sqrt{r r'} \left\{ \left(1 - \frac{\kappa^2}{2} \right) K(\kappa) - E(\kappa) \right\}, \tag{3.14}$$

where

$$\kappa^2 = \frac{4 r r'}{(r + r')^2 + (z - z)^2}, \tag{3.15}$$

and $K(\kappa)$ and $E(\kappa)$ are the complete elliptic integral of the first and the second kinds, respectively. The plasma current profile j_p^* is assumed as

$$j_p(\bar{\psi})^* = \left(R + \frac{\mu}{R} \right) \left(1 - \bar{\psi}^n \right)^m, \tag{3.16}$$

$$\mu = R^2 \left(\frac{1}{\beta_o} - 1 \right),$$

where $\bar{\psi} = (\psi - \psi_a)/(\psi_s - \psi_a)$ and ψ_a is the flux at the magnetic axis. The three parameters of β_o, n and m is parameterized with the three physical parameters, poloidal beta β_p, internal inductance l_i and safety factor at the magnetic axis q_a.

Assuming that the plasma is represented by a set of ring currents, Eqs. (3.13) and (3.13) are solved using the following iterative procedures:

1. set initial values of j_p to mesh points,
2. calculate ψ_p of each mesh point using Eq. (3.13),
3. calculate j_p of each mesh point using Eq. (3.17),
4. repeat the procedures 2 and 3 until

$$\left| \frac{j_\phi^n - j_\phi^{n-1}}{j_\phi^{n-1}} \right| \leq \epsilon, \tag{3.17}$$

where ϵ is an input tolerance.

In order to obtain an plasma equilibrium of the prescribed plasma boundary and plasma parameters, l_i and β_p, the currents in the field-shaping coils must be optimized. The desired plasma surface is represented by a set of M points r_j, z_j. At each step of the iteration, the values of ψ at each of these surface points is computed. The current in the coil I_k is changed to minimize

$$\epsilon_l = \sum_j w_j |\psi(r_j, z_j) - \psi_s + \sum_k G(r_j, z_j; r_k, z_k) - G(r_s, z_s; r_k, z_k) \delta I_k|^2, \tag{3.18}$$

where w_j is the weight function and δI_k is the correction of coil current. At the next step of the iteration, $I_k = I_k + \gamma \delta I_k$ is put, where γ is regularization parameter to suppress oscillations in I_k. Convergence loops of β_p and l_i are prepared in the same way.

3.2.2 Shielding Current Analysis in High Tc Superconductors

As for the shield current analysis in superconductors based on the flux flow creep model, there exists a code to which the current vector potential method (T method) is applied [41,42]. However, it is not efficient and facile to apply the code to the problems treated in this study. This is because it is not possible to directly treat multiply connected conductor such as ring with T method, which is ascribed to the gauges applied to the governing equation of T method [43]. In addition, formulation of T method is different from that of the modified inductance method, which make it difficult to couple the shielding current analysis and plasma equilibrium analysis. Therefore, code for shielding current analysis in superconductors is newly developed for this study [44].

Numerical Formulation

Shielding currents in the high Tc superconductors were evaluated based on the flux flow and creep model which properly describes quickly changing shielding currents in them as like this case. Constitutive relations between current density, $\boldsymbol{J}$, and electric filed, $\boldsymbol{E}$, based on the model are as follows [45]:

(1) The creep region ($0 \leq J \leq J_c$)

$$E(J) = 2\rho_c J_c \sinh\left(\frac{U_o}{k\theta}\frac{J}{J_c}\right)\exp\left(-\frac{U_o}{k\theta}\right), \tag{3.19}$$

(2) The flow region ($J_c \leq J$)

$$E(J) = E_c + \rho_f J_c(J/J_c - 1), \tag{3.20}$$

where E_c is the critical electric field, ρ_c the creep resistivity, θ the temperature, U_o the pinning potential, k the Boltzmann constant, ρ_f the flow resistivity and J_c the critical current density. Shielding currents in superconductors can be estimated by combining this constitutive relation with the conventional eddy current analysis. Therefore, in order to introduce the shielding current analysis to the system equations of Eqs. (1–4), Eq. (1) is changed as follows:

$$d\boldsymbol{\Phi}/dt + \boldsymbol{R}(\boldsymbol{I})\boldsymbol{I} = \boldsymbol{V} \tag{3.21}$$

where,

$$R_i \cdot I_i = \int_c E(J_i)dl. \tag{3.22}$$

Due to this change, Eq. (7) becomes nonlinear and the Newton-Raphson method was applied to solve Eq. (7).

Verification

Validity of the presented method was verified comparing the results with the experiment and computation based on the T method presented in ref. [41]. Fig.3.2.2 shows the schematic drawing of the configuration of the experiment and computation. It consists of an MPMG-processed cylindrical YBaCuO superconductor of 18 mm in diameter and 2.5 mm in thickness and a cylindrical permanent magnet of 25 mm in diameter and 22.5 mm in thickness, whose residual magnetization is 1.12 T. The magnet was fixed at the end of cantilever beam and moved from 25 mm to 0.5 mm in gap with the superconductors within 2 sec with constant speed. The physical parameters of the high Tc superconductor in the computation based on the presented method follow ones adopted in the computation of ref. [41]: $J_c = 1.3\times10^8 \mathrm{A/m^2}$, $U_o = 92\mathrm{MeV}$, $\rho_f = 7.62\times10^{-10}\Omega\mathrm{m}$ and $\rho_c = 7.69\times10^{-13}\Omega\mathrm{m}$. Fig. 3.4 shows the results of evolution of magnetic force. Three results, experimental one and computed ones based on the T method and the presented method, are agree with each other, which supports for the validity of the computational method presented here.

3.3 Verification of Stabilizing effect due to HTSC

3.3.1 Configuration

The EOB(End Of Burn) configuration of ITER TAC-8 outline design [1] was considered for the verification of feasibility of high Tc superconducting coils. The parameters of the

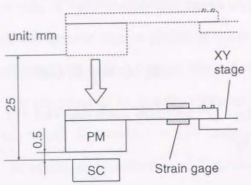

Figure 3.3: Schematic drawing of experimental setup.

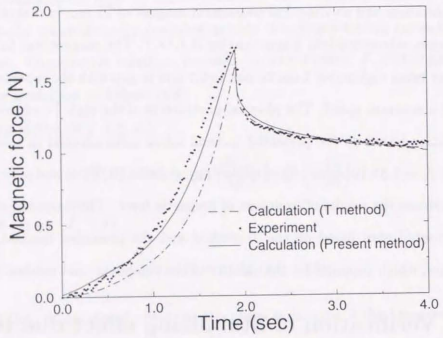

Figure 3.4: Electromagnetic force of high Tc superconductor.

plasma and structures are shown in Table 3.1 and their cross sections are shown in Fig. 3.5. In the computation, the conductive structures were modeled as an array of discrete conducting loops; the first wall, the back plates and vacuum vessel were approximated as axisymmetric rings of 25, 24 and 60, respectively to construct an equivalent electrical circuit. Growth time of the equilibrium with the conductors is valued at 1.23 sec, which agrees with the design report and validates the model of conductors surrounding the plasma.

An example of arrangements of the high Tc superconducting(HTSC) coils is also shown in Fig. 3.5. They are placed in the form of axisymmetric toroidal coils in the plasma periphery. Silver-sheathed Bi-2223 superconducting tape was considered as the material of high Tc superconducting coils. A picture of the 61-multifilamentary tape is shown in Photo 3.6. The tape is fabricated by the powder-in-tube methods and over 1000 m class tape is available as is mentioned in chapter 1. The parameters of Bi-2223 tape in the computation are shown in Table 3.2 and are assumed to be that of 100 m length tape which have been achieved in the current technology. The critical current density, J_c, of Bi-based tape at above 77.3 K (liquid nitrogen) drops abruptly in high magnetic field, which is the critical problem of its application at 77.3 K. Therefore, the dependence of J_c on the magnetic flux density must be taken into consideration. Here, the following empirical formula of the dependence were approximately applied to the computations [46].

$$J_c(B) = \frac{J_{co}}{\log(B_{self}/B_{irr})} \log(B/B_{irr}), \tag{3.23}$$

where B_{self} is the self magnetic induction, B_{irr} the irreversibility magnetic induction. B_{irr} of the Bi-2223 tapes measure 0.5 T. It should be noted that B in Eq.(3.23) is the component of magnetic induction perpendicular to the a-b planes of grain structures. Since the a-b planes of Bi-2223 tapes lie in the rolling plane of the fabrication process, the large toroidal magnetic field in the reactor does not affect the critical current of HTSC coils in the arrangement mentioned above. For example, the maximum poloidal field

perpendicular to the a-b planes of HTSC coils shown in Fig.3.5 amounts to 0.2 T, which does not change sharply due to the displacement of the plasma, and the critical current density of overall tape including Ag sheath is valued at 1.5 $\times 10^7 \mathrm{A/m^2}$.

3.3.2 Optimization of high Tc superconductors

Method of optimization

Method for optimizing the location and the size of the cross sections of the HTSC coils was explored to maximize the effect of the HTSC coils on the plasma stabilization. In this investigation, the following assumptions were taken to clarify the sensitivity of the optimized parameters of the system; (1) the number of the HTSC coil is two, (2) HTSC coils are located at the first wall, and (3) reference disturbance of the plasma is stepwise change of the poloidal beta ($\Delta\beta_p = -0.2$).

As for the poloidal locations of HTSC coils, four cases (case A, B, C and D) shown in Table 3.3 and Fig 3.7 were examined. Here, consider the system where the stabilizing coils are perfect conductors instead of superconductors. In this case, the system equation (3.3) becomes linear and the growth time of the plasma τ_p can be defined as $\max(\mathrm{eig}(L^{*-1}R))$, where eig(A) is the eigen values of matrix A. τ_p of each case is also shown in Table 3.3. Negative values of τ_p indicate that the system is stable. Figure 3.8 shows the displacement of the plasma current centroid in each case. From this figure, it is clear that time constants of four cases approximately correspond to the values of τ_p. Therefore, τ_p should be considered when the location of the HTSC coils is determined.

Next, the sizes of the cross section of the stabilizing coils were investigated in case A. If the coils of the perfect conductor were placed instead of superconductors in this case, the maximum current, I_{max}, in the coils amounts to 1.16 $\times 10^5$ A. When the area of the cross section of superconductor coils is larger than I_{max}/J_c, the flux flow phenomenon does not occur in the superconductor, that is, resistivity of shielding current is expected to be quite low. In Case A, $L_{\mathrm{m}} = \sqrt{I_{\mathrm{max}}/J_c}$ is 0.07 m. Figure 3.9 shows the relation

between the displacement of the plasma centroid and the size of the cross section of the superconducting coils. It indicates that the critical size concerning to the plasma stabilization is between 0.05 and 0.10 m, which is consistent with the value of L_{m} and supports for the above explanation.

Results

Based on the knowledge obtained in the above, optimization of the configuration of the HTSC coils was performed taking consideration of technological issues. Three cases were considered, i.e. Case 1 in which the coils are placed on the fast wall, Case 2 just behind the blanket and Case 3 behind the vacuum vessel. In each case, the number of coils was four and locations and sizes of the coils were optimized with regard to τ_p and L_{m}. The details of each cases are shown in Table 3.4 and Fig. 3.11. As for the disturbance of the plasma, we considered instantaneous β_p drop of 0.2 and li drop of 0.1 recovering in 5 sec, which is considered to be the most critical one for the design of ITER. Figure 3.11 shows the displacement of the plasma centroid in each case. In Case 3, the plasma is not stable because the response of the HTSC coils is spoiled due to the presence of the structures between the plasma and the stabilizer. The maximum displacement in Case 1 and Case 2 are 0.055 and 0.111, respectively and they are acceptable. However, in Case 1 where stabilizing coils are arranged on the first wall, there is a problem of large heat deposition and neutron flux. On the other hand, the flux decays to allowable level outside the blanket and it is concluded that Case 2 is acceptable from the technological viewpoint of the fusion reactor.

Next, Adopting Case 2, the size of the cross section of high Tc superconductors was optimized with respect to their stabilizing capacity. Four sizes: 5 cm $\times$ 5 cm, 10 cm $\times$ 10 cm, 20 cm $\times$ 20 cm and 30 cm $\times$ 30 cm were investigated and the results of them are shown in Fig. 3.12. In the case of 5 cm $\times$ 5 cm, the plasma touches the wall in a few second, while the positional instability is reduced compared with the case without high Tc

superconductors. Figure 3.13 shows the change in the total current and the profile of the current density of SC2 (see Fig.3.11) in this case. The shielding current over the critical current density flows in all area of the cross section due to the small size. Therefore, energy dissipation in HTSC coils will be large due to the flux flow phenomenon, resulting in deviation of the plasma position. On the contrary, in the case of 30 cm × 30 cm, the plasma almost recovers its original position very close to the base equilibrium. The change in the total current and the the current density profile of SC2 are also shown in Fig. 3.14. Efficient stabilization in this case is due to the fact that the shielding current density in the superconductors does not exceed the critical current density sharply as is shown in Fig. 3.14, that is to say, the long term phenomena of creep is dominant and the decay of shielding current is quite small. However, the plasma position does not recover exactly because of hysteresis and joule loss in the superconductors. Since the plasma almost recovers its position in the case of 30 cm × 30 cm, the case is adopted hereafter.

3.3.3 Verification of plasma stabilization due to HTSC

Fig.3.15 shows time evolution of various parameters of plasma in the case of 30 cm × 30 cm. Since ecrease of poloidal beta, β_p, is related to that of the plasma pressure, the centroid of the plasma current moves inward as shown in Fig.3.15-(a). This phenomenon causes the increase of the plasma current shown in Fig.3.15-(b) because the plasma tends to keep its poloidal flux. Owing to the disturbance, the displacement of the plasma centroid amounts to 5.7 % but it recovers to 1 % in 1 sec. Fig.3.16 shows the displacement of reference point at separatrix. The arrows in the upper part of Fig.3.16 represent the direction of the positive in the lower part of Fig.3.16. Reference points 2 – 5 moves toward the magnetic axis while the disturbance is applied and it is not concerned. On the other hand, reference points 1 and 6 moves toward the wall; the maximum displacement is 22.5 and 6.0 cm, respectively, which is allowable without any problem in view of technical point.

The results suggest possible avoidance of a vertical displacement event where major plasmas are supposed to touch the surrounding structures causing very severe damages on them and consequently this avoidance alleviates heavy technical design requirements on structural components.

3.3.4 Interaction of HTSC coils with poloidal fields during plasma start-up

It is highly required to overcome the problem that HTSC coils may consume the poloidal flux provided by CS coil and PF coils during plasma start-up. To meet this objective, twin loop configuration is adopted is shown in Fig. 3.17. In applying the external flux for the twin loop, electromotive force of the same direction is induced in the upper and lower loops, so that total electromotive force is canceled. On the other hand, during the plasma motion, electromotive forces induced in the two loops are opposite to each other and almost same stabilization is expected compared with that of independent two loop. Consequently, twin loop connection is expected to overcome the problem of flux consumption without losing the stabilizing effect. In this section, two issues related to the twin loop are examined: flux consumption and effect on the stabilizing effect.

Estimation of flux consumption

The flux consumption was estimated based on the start-up scenario of ITER. The wave form of PF coil currents of ITER are shown in Fig. 3.19 (a). Four loop of the high Tc superconductor are connected as Fig. 3.18 to form two set of twin loop (SC1 and SC4, SC2 and SC3 in Fig. 3.18). Two coils of each set are symmetric in position with regard to the equatorial plane. The evolution of flux consumption during start-up is shown Fig. 3.19 (c). In the case of twin loop connection only 3 % of the provided flux are consumed by high Tc superconducting coil, while flux consumption due to independent four loop amounts to 47 %.

Effect of twin loop connection on the stabilizing effect

Next, stabilizing effect was estimated in the case where twin loop connection is introduced. The connection of HTSC coils is the same as the above analysis. In this case, the evolutions of plasma displacement and shielding currents in HTSC coils are shown in Fig. 3.20. First point to be addressed is that the stabilizing effect of plasma is not deteriorated by introducing twin loop connection. Secondly, the induced currents in HTSC coils is decreased due to twin loop connection, which can be said a by-product of twin loop. This is because twin loop does not respond the change of plasma current. This by-product is desirable in the meaning that the cross section of HTSC coil can be saved and induced electromagnetic force is reduced. Consequently, it concluded that twin loop connection overcome the problem of flux consumption without losing the stabilizing effect and decrease of stabilizing current in HTSC is expected due to the twin loop.

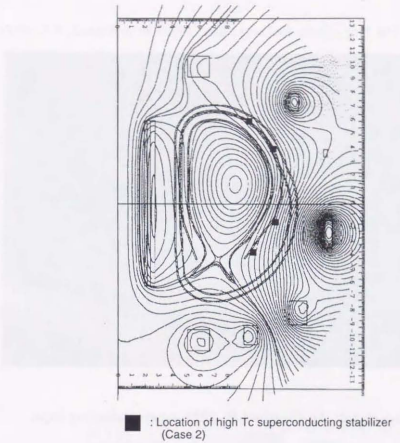

Figure 3.5: Configuration of ITER TAC-8 (EOB) and high Tc superconducting plasma stabilizer.

Table 3.1: Parameters of ITER/EDA TAC-8 (EOB).

Major radius R (m)	8.171
Minor radius a (m)	2.811
Plasma current I_p (MA)	21
Triangularity δ	0.326
Elongation κ	1.729
Poloidal beta β_p	0.892
Internal inductance li	0.901
Resistances (FW) R_{FW} ($\mu\Omega$)	100
Resistances (BP) R_{BP} ($\mu\Omega$)	8
Resistances (VV) R_{VV} ($\mu\Omega$)	13

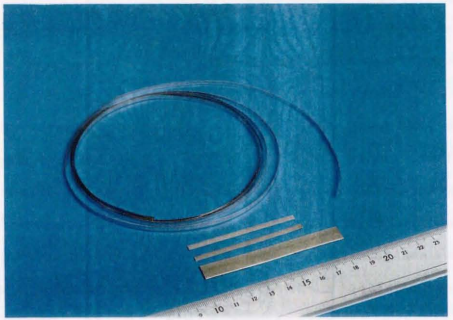

Figure 3.6: Ag-sheathed Bi-2223 superconducting tape.

Table 3.2: Parameters of HTSC tape.

Critical current density J_{co}(A/m^2)	2.7 $\times 10^8$
Flow resistivity ρ_f(Ωm)	1.2 $\times 10^{-9}$
Critical electric field E_c(μV/m) ($= \rho_c J_c$)	100
Pinning potential U_o(meV)	96
Temperature (K)	77
Number of filament	61
Ag ratio	2.5
Width (mm)	3.4
Thickness (mm)	0.24

Table 3.3: Location of HTSC coils (perfect conductor) and τ_p in each case.

	Location of stabilizing coils (R, Z)	τ_p (sec)
Case A	(9.83, −2.15) (9.25, 5.22)	−0.787
Case B	(10.37, −1.33) (10.72, 3.49)	−2.171
Case C	(8.31, −3.75) (8.30, 5.82)	−1.044
Case D	(10.98, −0.02) (11.13, 2.49)	3.46

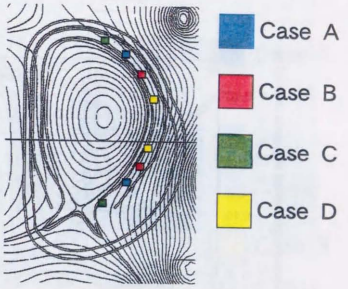

Figure 3.7: Location of HTSC coils (perfect conductor).

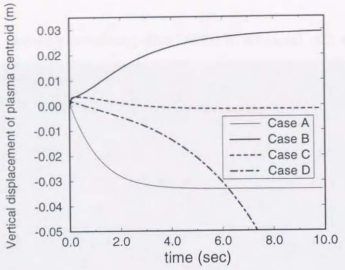

Figure 3.8: Relation between poloidal location of HTSC coils and its stabilizing effect on plasma.

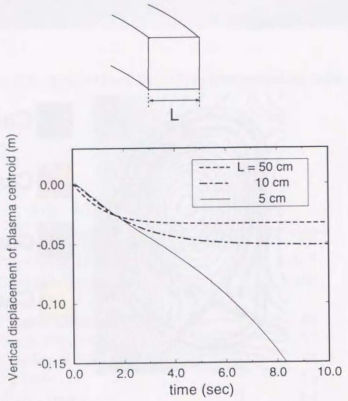

Figure 3.9: Relation between size of cross section of HTSC coils and its stabilizing effect on plasma.

Table 3.4: Location of HTSC coils and τ_p in each case.

	Location of stabilizing coil (R, Z)	τ_p (sec)
Case 1 (on FW)	(8.31, −3.75) (9.83, −2.15) (10.08, 4.43) (8.30, 5.82)	−0.698
Case 2 (outside BP)	(9.28, 6.04) (11.09, 4.08) (11.25, −1.23) (9.64, −3.43)	−0.916
Case 3 (outside VV)	(9.73, −6.32) (12.06, −4.05) (12.07, 3.31) (9.71, 6.36)	20.12

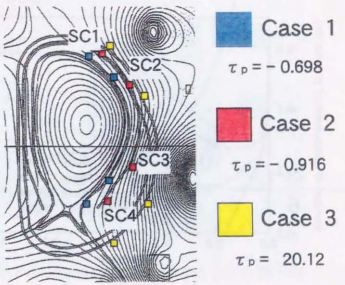

Figure 3.10: Location of HTSC coils.

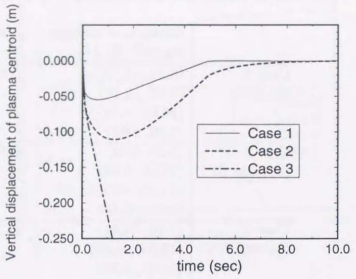

Figure 3.11: Relation between location of HTSC coils and its stabilizing effect on plasma.

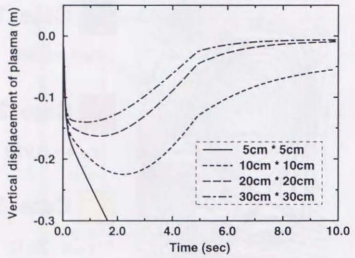

Figure 3.12: Relation between size of HTSC coils and its stabilizing effect on plasma.

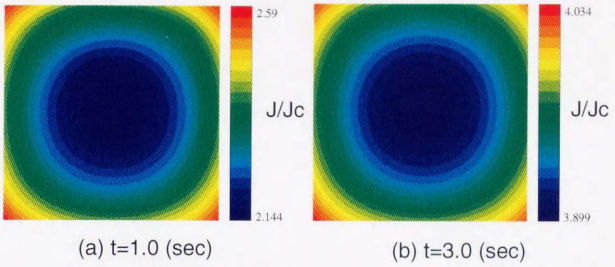

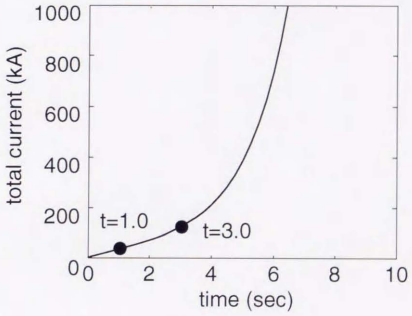

Figure 3.13: Evolution of current density profile in SC2 (5 cm × 5 cm).

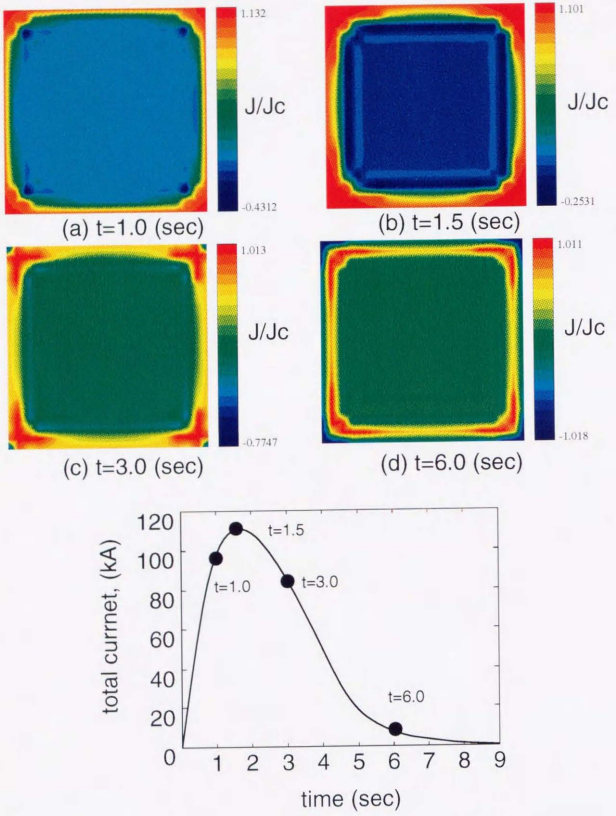

Figure 3.14: Evolution of current density profile in SC2 (30 cm × 30 cm).

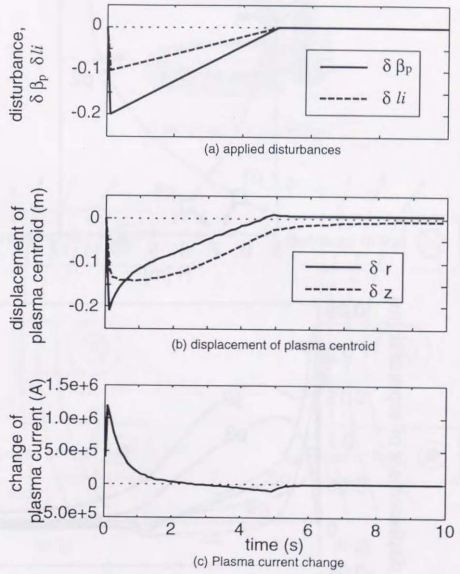

Figure 3.15: Evolution of plasma parameters in case D.

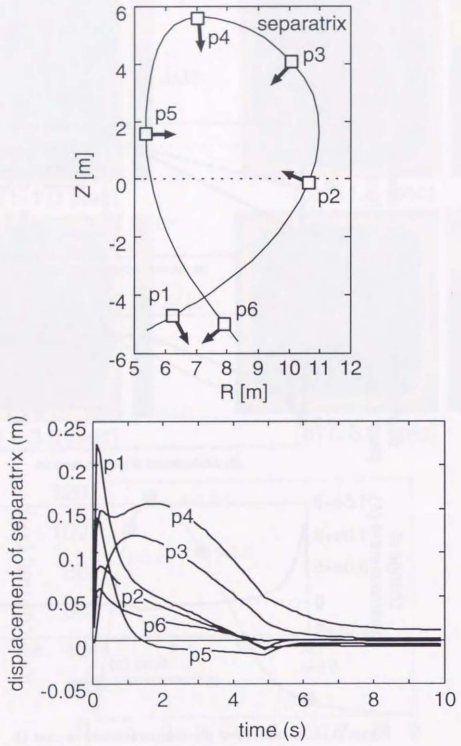

Figure 3.16: Displacement of reference points at separatrix.

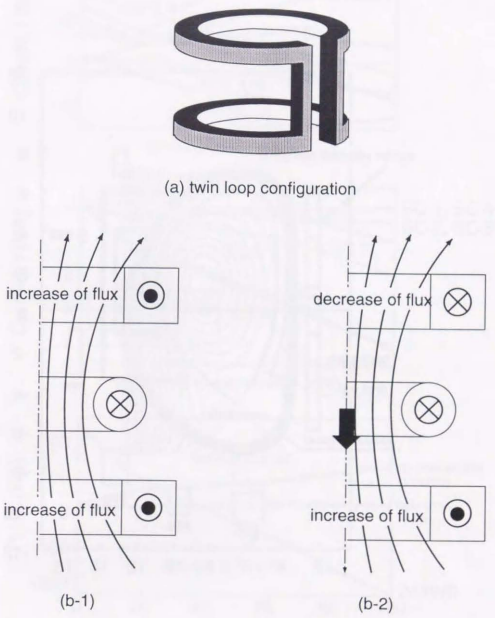

Figure 3.17: Schematic view of twin loop configuration.

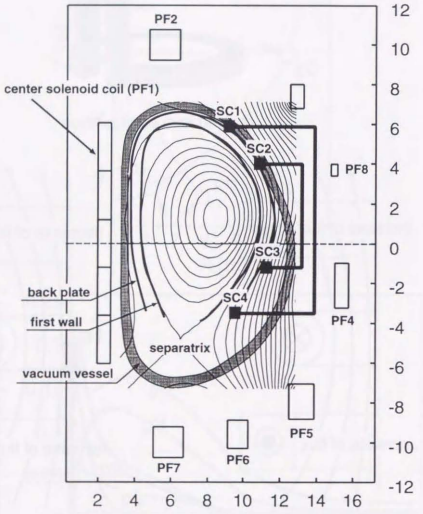

Figure 3.18: Configuration of connection of twinloop.

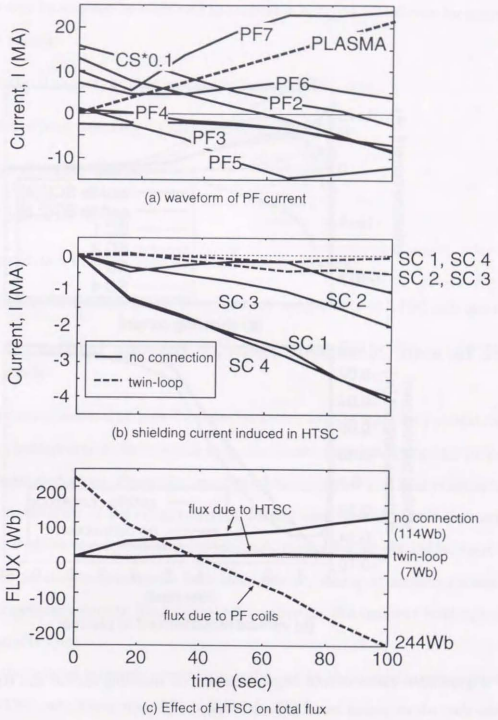

Figure 3.19: Evolution of parameters during plasma start-up.

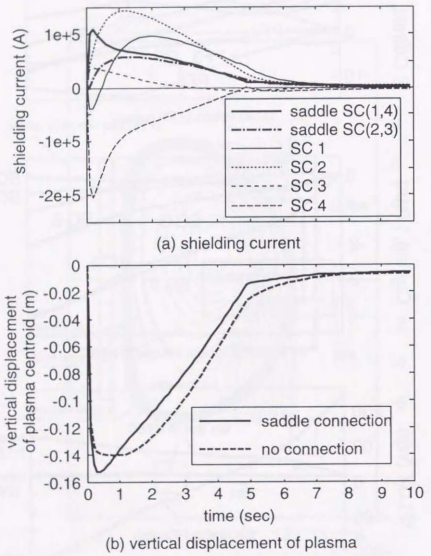

Figure 3.20: Effect of twin loop connection on shielding current and stabilization.

3.4 Technical Issues of HTSC coils

The following issues must be addressed and solved in applying HTSC coils for stabilization of fusion plasma:

1. structural support of electromagnetic force of HTSC coils,
2. effect of joint resistivity on stabilization of HTSC coils,
3. effect of nuclear heating,
4. AC loss in HTSC coils,
5. deterioration of HTSC coils due to neutron irradiation.

In this section, the above issues are examined and applicability of HTSC coils are verified.

3.4.1 Structural support of electromagnetic force of HTSC coils

Shielding current induced in high Tc superconductor couples with the poloidal field and generates electromagnetic force which may deteriorate the electromagnetic property of high Tc superconductors. Especially, mechanical tensile stress is of keen concern because it brings up decrease of the critical current density upon the high Tc superconductors and hence leads to the deterioration of the stabilizing effect of the HTSC coils. Here, the support for the electromagnetic force is considered, aiming at accommodation of the high Tc superconductors to keep their performance on the required level against the electromagnetic force.

Using the induced screening current J_{SC} computed by the coupled analysis of plasmas and the HTSC coils, electromagnetic radial and axial forces acting on the coils are given respectively by $F_r = \int_s 2\pi r J_{SC} B_z dS$ and $F_z = \int_s 2\pi r J_{SC} B_r dS$. Here, the integral is conducted over the cross-section of the coil, S and force, $\vec{F} = (F_r, F_\theta, F_z)$ and field, $\vec{B} = (B_r, B_\theta, B_z)$ are expressed in terms of the cylindrical system. The evolution of

electromagnetic force is shown Fig. 3.21: the maximums of F_r and F_z are about 6 MN (~600 tons) and 3 MN (~300 tons), respectively. Because tensile stress is serious in view of HTSC coil performance, as mentioned above, we pay attention to only the radial force and consider the support for it in the configuration shown in Fig. 3.22. The support is made of SUS316 and the following assumption is adopted; HTSC cable itself has no tolerance to deformation, hence, all hoop forces acting on the HTSC cable apply to an inner surface of the support structure. In this case, pressure to the inner surface amounts to 100 MPa and it induces the radial stress on SUS support and the strain on HTSC cable as is plotted in Fig. 3.23 against the various thickness of SUS support. The critical current density J_c is known experimentally to decrease to 90 % of it when 0.1 % of tensile strain is given. If thickness of a stainless steel case is 15 mm as the strain is 0.1 %. Taking a safety factor of 2, the thickness 30 mm is resulting in tensile strain of 0.05 %. Therefore, a design to accommodate these forces is possible without any difficulty.

3.4.2 Effect of joint resistivity on stabilizing effect

At present, technology of the superconducting joint of Bi-2223 multifilamentary superconducting tape is not established, while that of NbTi wire is achieved for MRI (Magnetic Resonance Imaging) magnets. Therefore, Ag-sheathed Bi-2223 tape must be connected with solder in order to fabricate HTSC coils. Fig. 3.24 shows the relationships between resistance of solder joint and joint length at 77 K [47]. If the joint length is more than 50 mm, the joint resistance of the order of $10^{-8}\Omega$ can be achieved. Based on these data, the effect of joint resistance on stabilization was estimated. Each turn of Ag-sheathed tape in HTSC coils was assumed to be connected at a solder joint of 50 mm in length. Fig. 3.25 shows the effect of joint resistance on stabilization and no large deviation due to the presence of the solder joints was observed. This is because the creep resistance of one turn Bi-2223 tape $\rho_c l/S$ (l is the length of one turn, S is the cross section of a tape) is approximately valued at $3 \times 10^5\Omega$ and addition of the joint resistance can be negligible.

3.4.3 Estimation of nuclear heating

Another concern is an increase of temperature in high Tc superconductors due to the nuclear heating which also have the possibility to degrade the critical current density resulting in the deterioration of the stabilizing effect of high Tc superconductors. Therefore, in order to predict the effect of nuclear heating on the stabilizing effect of high Tc superconductors, numerical analyses of neutron transport and heat conduction were carried out. In addition, based on the results of numerical analyses, an experiment was conducted using high Tc superconducting tapes and simulating the temperature rise due to nuclear heating.

Estimation of temperature rise due to nuclear heating

Numerical analyses of neutron transport were conducted at first with use of 1-D neutron transport code ANISN [48] supplemented by data library for multigroup constants and nuclear heating constant, Fusion-40 [49, 50]. The configuration of numerical analyses are shown in Fig. 3.26 with the results. High Tc superconducting coils are 30 cm in thickness and located just behind the back plate. Figure 3.27 shows the radial profile of nuclear heating rate. Nuclear heating amounts to 1.63×10^{-3} W/cc and 3.94×10^{-4} W/cc at the inner and outer surfaces of the high Tc superconducting coils, respectively.

Based on the heating density given by ANISN, numerical analyses of heat conduction in the high Tc superconducting coils were carried out with use of a conventional 2-D thermal analysis code. In the computation, thermal conductivity of Bi-2223 filament and Ag sheath are set to 2.0 W/m · K and 427.1 W/m · K, respectively [51]. The thermal analysis made clear the relation between the heating density in HTSC and temperature at the center of HTSC as shown in Fig. 3.28. If the nuclear heating at the outer surface of the back plate is adopted, the temperature rise of the tape is negligibly small like 0.05 K. As long as the HTSC coils are set at the rear side of the back plate, an effect of the

temperature rise on the behavior of the tape can be neglected as demonstrated in the following experiment.

Experiment

J-E constitutive relations were examined experimentally by giving thermal disturbances to the tape of 50 mm in length and induced electric field was measured by the four probe current method. An experimental set-up is shown in Fig.3.29. Taps were soldered to the central part of the tape at the distance of 15 mm for the E-measurement. A strain gauge of 120 Ω was attached to the tape as a heat source between the taps and a semiconductor thermometer was also attached to the tape surface below the strain gauge with thermal insulator to detect temperature change. The sample was cooled in liquid nitrogen. Transient current of pulse width of 6 sec was provided to the tape to simulate shielding current with use of the function synthesizer and the pulsed current supply.

Results of J-E relations are also shown with parameter of temperature rise in Fig.3.30, where are demonstrated decrease of the critical current density corresponding to $E = 0$ and constant flow resistivity corresponding to the slope of a curve . In order to know influence of temperature increase by 2K on the stability behavior of the plasmas, the coupled analysis was conducted with use of the J-E relation obtained experimentally. Results show that no significant change is observed on the stability behavior of the ITER plasmas for temperature rise up to 20K. Little change is distinguished at T=105.1 K in Fig.3.31. This shows not only a very big margin for thermal instability of superconductivity compared with low Tc superconductors but also electromagnetic margin for the HTSC tapes.

Estimation of life time of HTSC coils

Figure 3.32 shows the radial profile of neutron flux in presence of HTSC coils in ITER, which is calculated with ANISN. Neutron flux amounts to 2.601 $\times 10^{11}$n/cm^{2}sec and 7.23 $\times 10^{10}$n/cm^{2}sec at the inner and outer surfaces of the high Tc superconducting coils,

respectively. On the other hand, the critical fluence for neutron irradiation is the order 10^{18} in the case of Bi-based superconductors, as is mentioned in chapter 1. Therefore, life time of HTSC coils can be estimated approximately as (critical fluence)/(flux) $\sim$ 3.8 $\times 10^6$ seconds, which corresponds to 3800 shots for the ITER plasma operation.

3.4.4 AC loss in HTSC coils

AC loss in HTSC coils must be estimated to consider the capacity of cryocooler for liquid nitrogen. AC loss P was computed, following

$$P = \int_V \boldsymbol{J} \cdot \boldsymbol{E} dV. \tag{3.24}$$

Figure 3.33 shows the evolution of AC loss in SC2 of the HTSC coils (see Fig. 3.11), which experiences the largest AC loss during the reference disturbance. The maximum AC loss in SC2 amounts to 7.59 kW.

Next, electric power for removal of heat in the HTSC coils is considered. Possible heats originate from nuclear heating and AC loss; the former is steady and the latter is transient. As is disscussed above, the maximum nuclear heating rate in HTSC is 1.63 $\times 10^{-3}$ W/cc. Therefore, the nuclear heating amounts to 37 kW in the whole system of HTSC coils. On the other hand, heating due to AC loss, which is transient, amounts to about 30 kW. The efficiency of the current cryocooler for liquid nitrogen is about 10. Therefore, electric power for removal of heat is estimated at 670 kW in the maximum, which is significantly small.

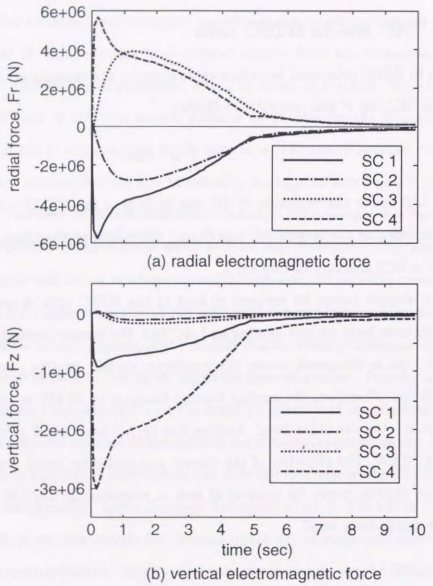

Figure 3.21: Evolution of electromagnetic force acting on high Tc superconductor.

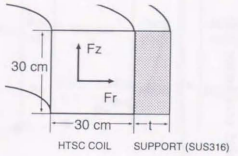

Figure 3.22: Schematic drawing of SUS316 support for electromagnetic force.

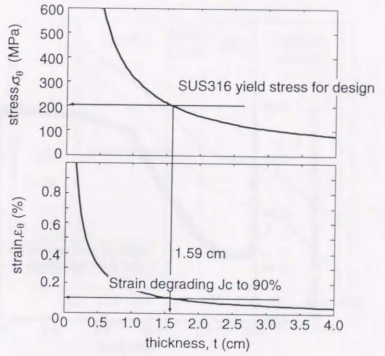

Figure 3.23: Stress and strain at support structure and high Tc superconducting tape.

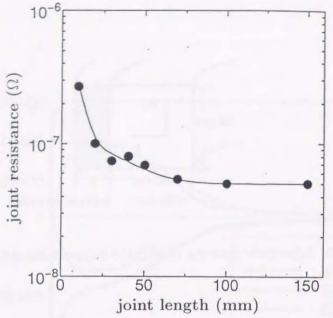

Figure 3.24: Relationships between resistance of solder joint and joint length at 77 K.

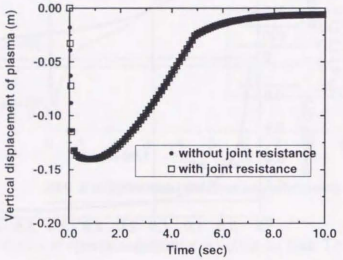

Figure 3.25: Effect of joint resistance in HTSC coils on plasma stabilization.

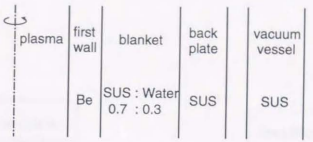

Figure 3.26: Configuration of neutron transport calculation.

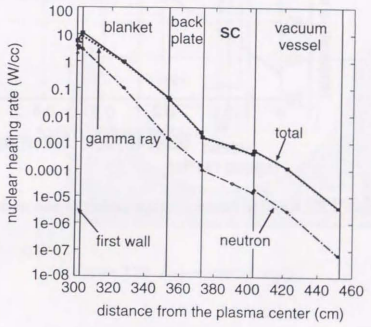

Figure 3.27: Radial profile of nuclear heating rate in presence of HTSC coils in ITER.

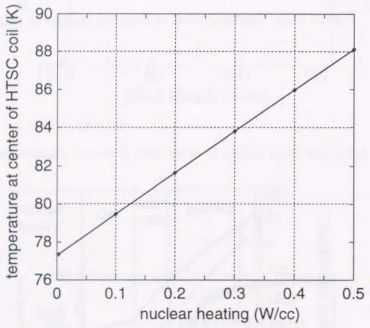

Figure 3.28: Relation between temperature rise and nuclear heating.

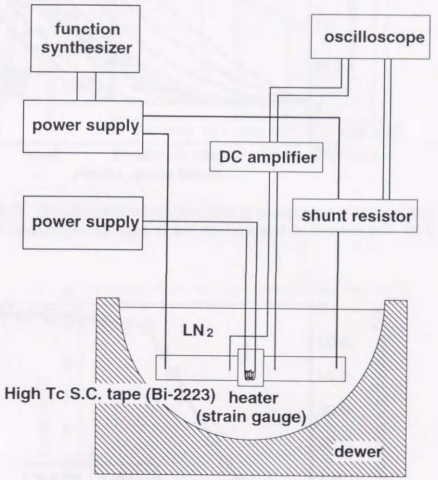

Figure 3.29: Experimental setup.

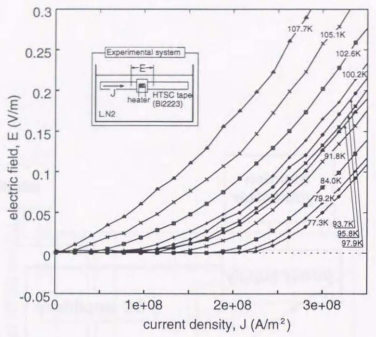

Figure 3.30: Dependence of temperature rise in high Tc superconductor sample on J-E curve.

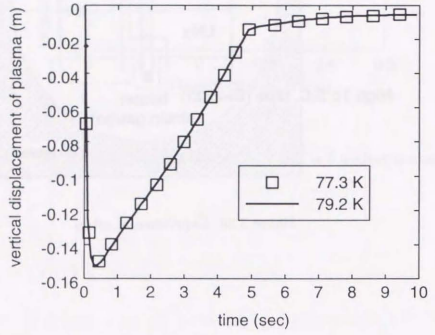

Figure 3.31: Effect of temperature rise on stabilization of plasma.

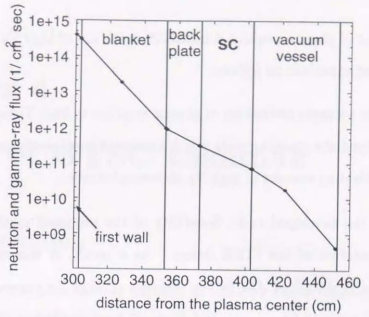

Figure 3.32: Radial profile of neutron flux in presence of HTSC coils in ITER.

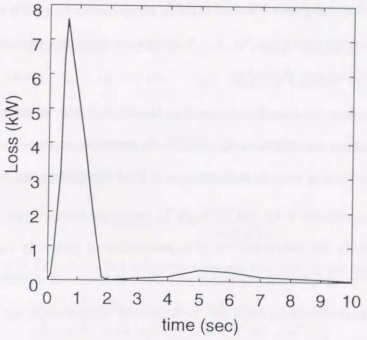

Figure 3.33: Evolution of AC loss in SC2 of the HTSC coils

3.5 Conclusion

Improvement of plasma positional instability with use of high Tc superconducting coil is proposed and examined as follows:

- For the accurate estimation of plasma response to high Tc superconducting coils, we developed the coupling code which consistently solves dynamic plasma equilibrium and shielding current in high Tc superconductors.
- With the developed code, feasibility of the proposed method is examined in the configuration of the ITER design. As a result, it was confirmed that unstable plasma is stabilized due to the presence of high Tc superconducting coils even if disturbances of $\delta\beta_p = -0.2$ and $\delta li = -0.1$ are applied at the same time.
- Applicability of high Tc superconductors to fusion reactor environment is investigated as follows;
  - Electromagnetic force on high Tc superconducting coils is calculated and design support structure for it. A design to accommodate these forces is possible without any difficulty.
  - Nuclear heating due to neutron irradiation was estimated with use of the 1-D neutron transport code ANISN. Supposed temperature rise in high Tc superconducting coils is estimated as 2 K at the maximum.
  - Experiment with use of high Tc superconductor tape was carried out to estimate the deterioration of superconductor property due to temperature rise. From the results, it turns out that decrease of stabilizing effect of high Tc superconducting coils due to supposed temperature rise is negligible.

  It follows form the results that high Tc superconductors provided by the current technology is applicable to the proposed method.

Chapter 4

Design of HTSC tokamak

4.1 Introduction

Vertical elongations of plasma cross sections in tokamak fusion reactors are desirable as is addressed in the previous chapter. Here, this fact is discussed again in more details to clarify the motivation of the design with use of high Tc superconductor.

The equilibrium toroidal plasma current can be approximated by the formula [52]:

$$I_p(\mathrm{MA}) = [5a(\mathrm{m})B_0(\mathrm{T})/q_a][C_I\epsilon/(1-\epsilon^2)^2][(1+\kappa^2)/2] \tag{4.1}$$

where B_0 is the vacuum toroidal field at the plasma major radius R, q_a the edge safety factor, $\epsilon = 1/A$ and $C_I = 1.22 - 0.68\epsilon$. This equation implies that the greater the elongation is the greater plasma current is permitted under the same constraint of the safety factor, which leads improvement of the important plasma quantities. In applying the Troyon scaling, the maximum beta is expressed as [53]

$$\beta_{max}(\%) = 2.8\frac{I_p(\mathrm{MA})}{a(\mathrm{m})B_0(\mathrm{T})} \tag{4.2}$$

Substituting this into Eq. (4.1), the relation between the maximum beta and elongation is obtained as:

$$\beta_{max}(\%) = 14/q_a[C_I\epsilon/(1-\epsilon^2)^2][(1+\kappa^2)/2] \tag{4.3}$$

This relation was plotted in Fig. 4.1 and it can be recognized that the larger beta is expected with increasing elongation.

Another important plasma quantity is energy confinement time. A scaling law of energy confinement in ITER is expressed as follows [54],

$$\tau_E^{ITER89-P} = 0.048 I_p^{0.85} R^{1.2} a^{0.3} \kappa^{0.5} n_{20}^{0.1} B^{0.2} A_i^{0.5} P^{-0.5}. \quad (4.4)$$

It has the direct dependency of elongation as $\kappa^{0.5}$ and the indirect one as $I_p^{0.5}$. Therefore, energy confinement is also improved as increasing elongation. Consequently, high elongation enables the important plasma quantities to be improved leading to compact machine.

However, elongated plasma has a strong susceptibility to axisymmetric instabilities and elongations are usually restricted to the range $\kappa \leq 2$ to prevent this mode from occurring. This is why the elongation is determined taking into the consideration of trade-off between its merits and drawbacks. Application of high Tc superconductors has the possibility to realize the high elongated tokamak free from the axisymmetric positional instability. An example of conceptual designs with use of high Tc superconductors, HTSC tokamak, will be introduced in the following and the emphasize will be on the possibility to design smaller ignited tokamak.

4.2 Design procedure and formulae to determine the plasma parameters

4.2.1 I-A-B_{tf}-κ analysis methodology

In arriving at an optimum design point of a HTSC tokamak, we must meld the main feature of HTSC tokamak (highly elongated plasma, small size device, ignition, etc.) with the present physical paradigm and engineering database and figure design window bounded by various constraints. For this purpose, we employ the I-A-B_{tf}-κ analysis methodology which was introduced in the ITER Conceptual Design Activity [55]. Fig. 4.2 shows schematically the four-dimensional I-A-B_{tf}-κ space where the axes are plasma current (I), aspect ratio(A), peak field at the TF coils (B_{tf}), and elongation (κ). If the

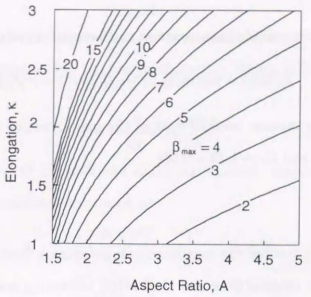

Figure 4.1: Dependence of aspect ratio and elongation on beta limit.

following two parameters are defined: (1) the minimum safety factor at the plasma edge, (2) radial build between plasma and inner leg of TF coil which includes inboard scrapeoff layer, first wall, inboard blanket and vacuum vessel, then, the grid point in the phase space corresponds to unique machine with a unique specifications of major radius , minor radius, axial field, TF and CS magnet geometries, etc.. Allowable designs lie in the area bounded by the surfaces drawn based on the constraints. This constraint surfaces are determined by taking into account the consideration of device mission, physical data base, and technology.

4.2.2 Physics and technological model and constraints

The following models and constraints are employed to specify the machine parameters in each grid point in the I-A-B_{tf}-κ space and draw the constraint surfaces.

Plasma current

The equilibrium toroidal plasma current can be approximated by the formula:

$$I_p(\mathrm{MA}) = [5a(\mathrm{m})B_0(\mathrm{T})/q_a][C_I\epsilon/(1-\epsilon^2)^2][(1+\kappa^2)/2] \tag{4.5}$$

where B_0 is the vacuum toroidal field at the plasma major radius R, q_a the edge safety factor, $\epsilon = 1/A$ and $C_I = 1.22 - 0.68\epsilon$.

Beta limit

A simple scaling law for the maximum volume-average beta that can be reached before the macroscopic external kink and ideal-MHD ballooning instabilities is

$$\beta_{max}(\%) = (2.5 \sim 3.5)\frac{I(\mathrm{MA})}{a(\mathrm{m})B_o(\mathrm{T})}. \tag{4.6}$$

This form of the beta limit, known as Troyon limit, has been observed experimentally and suggested by theoretical studies.

Plasma power balance

A criterion for an ignition condition is described as

$$P_\alpha + P_{OH} - P_{cond} - P_{br} - P_{syn} + P_{aux} = 0 \tag{4.7}$$

where P_α: alpha particle heating, P_{OH}: Ohmic heating, P_{cond}: heat conduction loss, P_{br}: Bremsstrahlung radiation loss, P_{syn}: Synchrotron radiation loss and P_{aux}: auxiliary heating. Each term in Eq.4.7 is based on the plasma zero dimensional model which was employed in the early stage of ITER Conceptual Design Activity [54]. These terms are function of the ion density (n) and temperature (T). Eq. (4.7) is an energy balance for continuous operation, so that combination of (n, T) satisfying the condition, $P_{aux} = 0$, secure ignition. A scaling law of energy confinement in ITER is expressed as follows,

$$\tau_E^{ITER89-P} = 0.048 I_p^{0.85} R^{1.2} a^{0.3} \kappa^{0.5} n_{20}^{0.1} B^{0.2} A_i^{0.5} P^{-0.5}. \tag{4.8}$$

Toroidal field coil

TF coil shape in this design follows the pure tension curve, which can be approximated using the analytic formulas [56]. In the configuration shown in Fig. 4.3, tension T is simply expressed as

$$T = \frac{\mu_o N_c I_c^2}{8\pi} \ln\left(\frac{R_2}{R_1}\right), \tag{4.9}$$

where N_c is the number of TF coils and I_c the coil current. Employing the tension, the inner radius of coil curvature is expressed as

$$\rho_i = \frac{1}{c}\left(\frac{2\pi a^2 b^2 T}{\mu_o N_c I_c^2} - e\right) \qquad [b \neq 0], \tag{4.10}$$

$$\rho_i = \frac{4\pi R_i T}{\mu_o N_c I_c^2} - \frac{a}{3} \qquad [b = 0], \tag{4.11}$$

where a, b, c, d and e are

$$\begin{aligned} a &= \rho_o - \rho_i, \\ b &= \cos\theta, \\ c &= \ln\left\{\frac{R_i ab}{R_i}\right\}, \\ d &= cR_i - (a - ac)b, \\ e &= \frac{a^2 b}{2} + (a - ac)R_i - \frac{c}{b}R_i^2. \end{aligned}$$

While TF coils are subjected to various kind of electromagnetic force, for simplicity we will only pay attentions to the tension and consider the mechanical support for it. Therefore, the cross-section area of conduit is

$$S_{\mathrm{conduit}} = T/\sigma, \tag{4.12}$$

where σ is yield stress for design.

Center solenoid coil

Design of the center solenoid coil is determined by the volt-second consumption, incorporating the constraints due to mechanical stress and critical magnetic field of conductor.

The volt-second consumption can be derived by the plasma circuit equation as

$$L_p I_p + C_{\rm ejima}\mu_o R_p I_p + V_{\rm loop} T_{op} = 2M_{OH,p} I_{CS\max} \tag{4.13}$$

where L_p is the self inductance of the plasma, $C_{\rm ejima}$ the Ejima coefficient [58], $V_{\rm loop}$ the one-turn voltage of the plasma at the flat top, T_{op} the flat top duration, $M_{OH,p}$ the mutual inductance between the plasma and the CS coil, and $I_{CS\max}$ the maximum CS coil current. For the specified T_{op}, the values of $M_{OH,p}$ and $I_{CS\max}$ must be optimized taking into the consideration of mechanical stress and critical magnetic field of conductor. As for the mechanical stress, if the CS coil is designed to be self-supporting for the hoop forces, tensile stress of conduit materials by hoop force is then calculated by

$$\begin{aligned} \sigma &= \frac{B_{\max} J_{CS}(R_{out} - R_{in})}{f} \\ f &= \frac{\text{conduit area}}{\text{conductor area}} \end{aligned} \tag{4.14}$$

4.2.3 Design window in I-A-B$_{tf}$-κ space

As 4-D surfaces can not be visualized, we consider 2-D I-A plot of plasma current versus aspect ratio at constant values of B_{tf} and κ. Here, primary reactor parameters to identify are selected as follows: R (major radius), a (minor radius), A (aspect ratio), κ(elongation) and δ (triangularity), B_{tf} (maximum toroidal magnetic field at TF coils), B_o (toroidal magnetic field at plasma axis), q_ψ (safety factor), I_p (plasma current), n (density of ions and electrons), T (temperature of ions) and β (beta value). In each grid in 2-D I-A space, R, a, A, κ, B_{tf}, B_o and I_p are specified using Eq.(4.5) and relation between B_{tf} and B_o,

$$B_0 = \frac{B_{TF}(R - a - d)}{R}. \tag{4.15}$$

In order to determine the design, two constraints is applied: the ignition constraint and the radial build constraint. The former constraint surface is determined by the plasma power balance expressed as Eq.(4.7) incorporating the beta limit of Eq. (4.6). The latter constraint is expressed as

$$R - a \geq R_{CS} + t_{TF} + t_{\rm shield}, \tag{4.16}$$

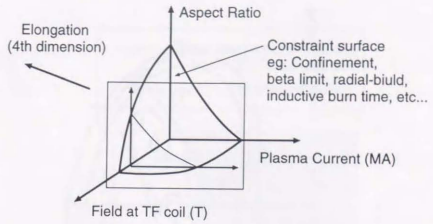

Figure 4.2: Schematic drawing of I-A-B phase space.

where the outer radius of CS coil R_{CS} and thickness of inner leg of TF coil. t_{TF} are determined by the design criteria mentioned in the above.

4.3 Results

4.3.1 Determination of plasma parameters

Firstly, we determined apriori the basic parameters, κ=2.3, B_{tf}=12.5(T), $q_\psi > 3.0$, and $t_{\rm shield} = 1.05$ m with intention of a smaller tokamak of reasonable fusion power. Here, the elongation was chosen to the maximum value in the range that plasma positional stability is secured with HTSC coils after some iteration of plasma stability analysis was made.

The $I_p - A$ space of HTSC tokamak ($\kappa = 2.3$) is shown in Fig. 4.4(a) with parameters of major radius determined by Eq.(4.5) together with that of ITER (Fig. 4.4(b)). The hatched region in the figure corresponds to the possible design window which is bounded by consideration of Eqs. (4.7), (4.6) and (4.16). It can be easily recognized that major radii in the possible region of HTSC tokamak are much smaller than that of ITER. We determine $I_p = 18$(MA) for $A = 3.5$ and $R = 5.34$(m) as the design point. This is very small compared with the size of the present ITER.

Then, we have to determine plasma parameters so as to secure an ignited condition.

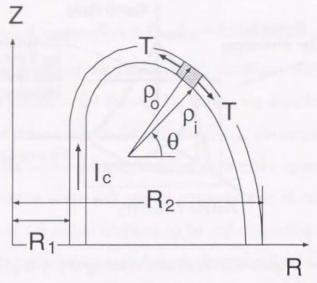

Figure 4.3: Geometry of TF coil for calculation.

For this purpose, a POPCON(Plasma OPeration CONtour) diagram [57] based on Eqs. (4.7) and (4.8) is shown in Fig.4.5 together with beta limit based on Troyon scaling. Digits in the figure are an additional heating power, P_{aux}, so that domain bounded by two curves, $g = 2.2$ and $P_{aux} = 0$, gives possible (n, T) sets of an ignited operation. If we take a fusion power of 500 MW, contour line of 500 MW gives $< n >= 0.9 \times 10^{20} 1/\mathrm{m}^3$ and $< T >= 13$ keV as the cross point with the curve of $P_{aux} = 0$. For this condition, each term of Eq.(4.7) are evaluated as $P_\alpha = 106, P_{OH} = 1.8, P_{cond} = 83.1(\tau_E = 3.67$ sec) and $P_S + P_B = 24.7$ in unit of MW.

4.3.2 Analyses of plasma equilibrium and positional stability

The elongation of HTSC tokamak is set to higher value than that of ITER, so that it is highly required to investigate whether or not the plasma equilibrium condition is satisfied and its positional stability is secured. For this purpose the two dimensional analysis code, "SYSTEQ", was used to find the location of PF coils and to determine magnitudes of the coil currents for equilibrium state plasma. The results are shown in Fig. 4.6. Primary

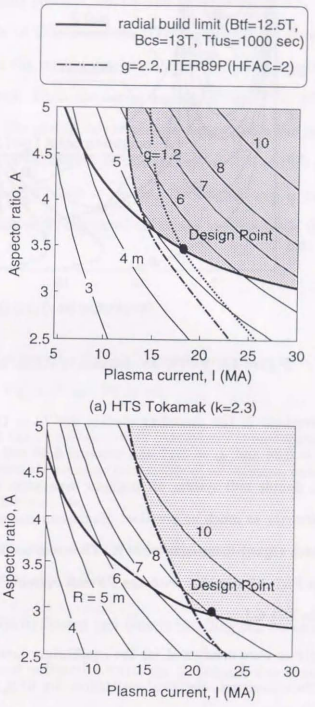

Figure 4.4: Decision of operation point in I-A space.

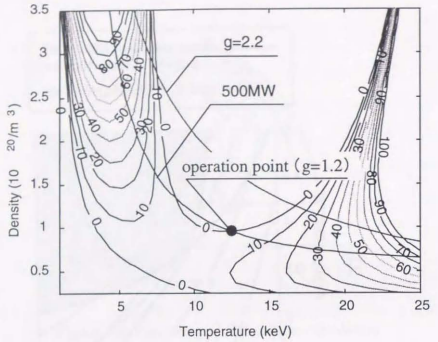

Figure 4.5: POPCON diagram of HTSC tokamak.

parameters determined in the preceding section are $I_p = 18.0$ MA, $R = 5.3$ m, $A = 3.5$, $\kappa = 2.3$, $\delta = 0.24$ and $q_\psi = 3.17$ and poloidal field coil system is determined with SYSTEQ. Here, double null system of magnetic separatrix is adopted for reduction of heat flux on a divertor as much as possible. Magnetomechanical systems of the machine are symmetric with regard to an equator of it. The cross section of magnetic flux contour lines is shown in Fig. 4.6 together with the PF coil currents. Total stored energy in the PF coil system is 2.71 GJ.

Stability analyses were conducted for the equilibrium arrangement obtained by SYSTEQ code. In these analyses, electrical resistances are 67.9, 5.63 and 9.41 ($\mu\Omega$) for the first wall, the back plate and the vacuum vessel, respectively. These values are evaluated on the data base given in the ITER design. The decay constant of plasmas is very short as 66 msec while ITER is longer as 1.2 sec. In order to improve the plasma positional instability, four pairs of HTSC coils are installed at the back plate as shown in Fig.4.7

after some iteration was made to optimize the location and the number of the coils. Displacement of the plasma centroid against the disturbance of $\Delta\beta_p = -0.2$ are evaluated with the coupled code of TOFU and the HTSC code and are shown in Fig.4.8. For reference, Fig. 4.9 shows the vertical displacement of the plasma centroid in the case where no HTSC coil is placed. From the comparison, it is clear that HTSC coils successfully stabilize the plasma. The motion of the plasma separatrix in the presence of HTSC coils is shown in Fig. 4.10. The plasmas at reference points P1 and P4 move toward the first wall by 16 cm, but do not touch it because the original gap is sufficient, 25 cm. The above results imply that high elongated tokamaks are feasible if HTSC stabilizing coils are applied.

4.4 Conclusion

The following remarks are drawn from the comparison between HTSC tokamak and ITER/EDA shown in Fig. 4.11 and Table 4.4:

1. Smaller tokamak can be designed with parameters of moderately lower fusion power of 500 MW, reduced stored magnetic energy of coil system, easy handling of thermal deposition at a divertor, *etc.*.

2. Additional heating power required for L/H transition can be reduced significantly due to the smaller major radius.

3. Fabrication can be facilitated and remote handling can be accommodated easily.

4. Amount of low level radioactive waste can be reduced due to small scaled structure.

5. Volume of the nuclear island of the HTSC tokamak is roughly one-third of ITER.

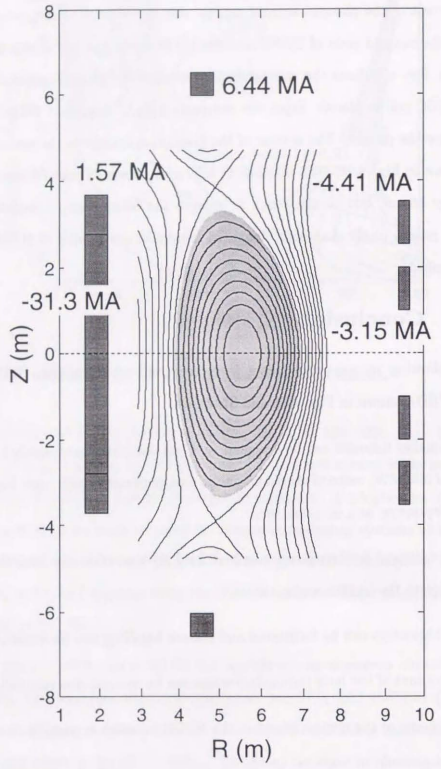

Figure 4.6: Result of plasma equilibrium analysis.

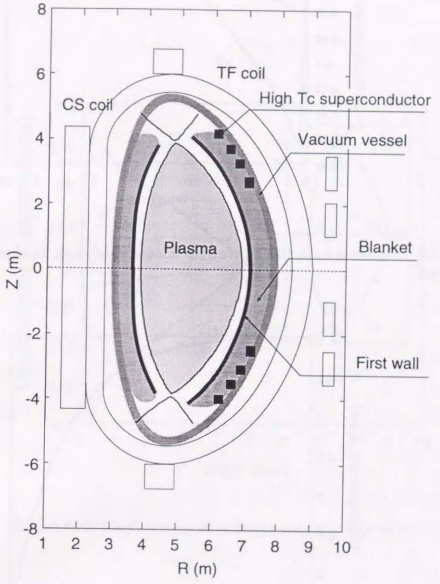

Figure 4.7: Configuration of positional stability analysis.

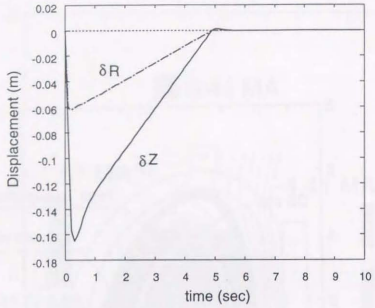

Figure 4.8: Displacement of plasma centroid in case where high Tc superconducting coils are placed.

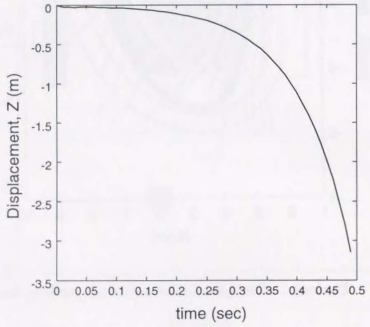

Figure 4.9: Vertical displacement of plasma centroid in case where no high Tc superconducting coil is placed.

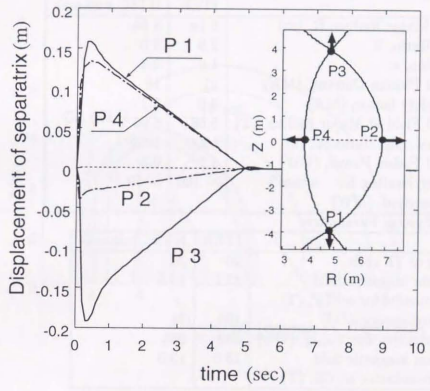

Figure 4.10: Displacement of reference points at separatrix.

Table 4.1: Comparison of design parameters between HTSC tokamak and ITER/EDA.

(a) Major Design Parameters

	ITER	HTSC tokamak
Plasma Major Radius, R, (m)	8.14	5.34
Aspect Ratio, A	2.9	3.5
Elongation, κ	1.6	2.3
Nominal Plasma Current, (MA)	21	18
MHD safety factor, (MA)	3.0	3.2
Toroidal Field at Major Radius, (T)	5.68	6.05
Reference pulse duration, (s)	1000	1000
Nominal Fusion Power, (GW)	1.5	0.5
Auxiliary Heating for L/H transition, (MW)	~ 100	~ 40

(b) Coil System Parameters

	ITER	HTSC tokamak
Number of TF coils,	20	20
Maximum magnetic field at superconductor at TF, (T)	12.5	12.5
TF Stored energy, (GJ)	103	31
Total inductive flux swing, (Wb)	530	285
Maximum magnetic field at superconductor at CS, (T)	13.0	13.0

(c) Parameters of Plasma Facing Components

	ITER	HTSC tokamak
Nominal Wall Loading, (MW/m^2)	~ 1.0	~ 0.76
Total surface heat loads, (MW)	< 300	< 100
Local thermal load at normal operation condition, (MW/m^2)	5	~ 1.8

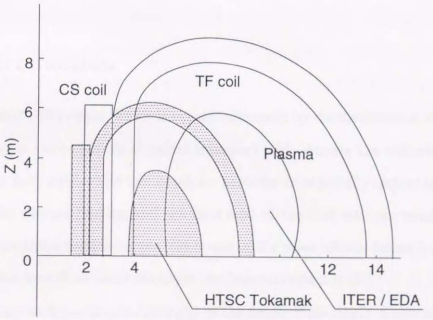

Figure 4.11: Comparison of size between HTSC tokamak and ITER/EDA.

Chapter 5

Reduction of Toroidal Ripple with use of HTSC

5.1 Introduction

The toroidal field (TF) ripple, which is caused inherently by the discreteness of the magnet system, promotes various kinds of radial transport [59]. Among the unfavorable results caused by the field ripple, the loss of alpha particles is especially important when the efficiency of the plasma heating and the heat load of the first wall are considered. The reduction of the alpha particle ripple loss is one of the most critical issues for design of a tokamak reactor as well as other magnetic confinement systems [60].

Ripple transport depends quite strongly on the depth of the ripple, which is determined by the design, primarily by the number of the toroidal field coils. Therefore, the ripple transport can be suppressed by increasing the number of the TF coils. On the contrary, the number of the TF coils is desired to be reduced because the smaller number of TF coils allows the following improvements:

1. Neutral beams can be injected tangentially, which is favorable from the viewpoint of the current drive efficiency.

2. Larger, higher conductance vacuum ports can be used so that fewer units are required.

3. The shielding and vacuum vessel can be installed in fewer, larger pieces with large savings in fabrication costs.

4. Fewer TF coils lead to savings in the cost of cryostats and leads.

5. Access for maintenance is decisively better. Remote maintenance equipment can be simpler and maintenance time shorter.

6. Assembly of the reactor is decisively easier and faster.

Consequently, the TF ripple has to be reduced without increasing the number and the size of TF coils. There are several ways to overcome this difficulty. One of them is to use ferromagnetic balls in the vacuum vessel under the outer TF coil legs. But the magnetization of the balls will be saturated because of the high toroidal magnetic field, and then they can not reduce the TF ripple significantly.

In this chapter, a new method to reduce the TF ripple with use of bulk high Tc superconductors is proposed. They can behave as ferromagnetic or diamagnetic materials depending on their magnetic hysteresis. In addition, they can trap magnetic field in their body more efficiently than ferromagnetic materials. Therefore, if superconductors are appropriately arranged and magnetized, they possibly decrease the TF ripple. The outstanding feature of this method can be stated as follows;

- The superconductors do not saturate magnetically if their size is large enough, contrary to ferromagnetic materials.
- They do not need electrical feed like correction coils.

In this chapter, the feasibility of ripple reduction with use of high Tc superconductors is verified through experiment and numerical analysis. In addition, parameter survey of the superconductors is performed in the configuration of the outline design of ITER, and a guideline of design for the superconductors is presented.

5.2 Experiment

5.2.1 Description of experiment

The experimental arrangement is shown in Fig. 5.1. The experiment was performed to investigate how the superconductor reforms the rippled field between the pole faces of the normal magnet. The magnet can generate the maximum flux density of 2.0 T. The high Tc superconductor is a QMG-processed YBaCuO sample [18], and rectangular shape, 30.8 mm in width and length and 10.5 mm in height. The superconductor was magnetized by zero-field cooling process as follows. The superconductor was immersed and cooled in liquid nitrogen at location "A" (see Fig. 5.1) where magnetic field was almost zero. Next the superconductor was moved from location "A" to "B", resulting in magnetization of the superconductor. The flux density between the magnetic poles was measured by a Hall probe.

Numerical analysis of magnetic induction due to HTSC in this configuration was also carried out. In order to compute the magnetic induction, shielding current in HTSC is computed by applying the current vector potential method (see later with respect to the detail). In the computation, the measured magnetic field data were employed as the exciting field of shielding current in HTSC.

5.2.2 Results

Fig. 5.2 shows a profile of the magnetic induction at Y = 9 (mm), Z = 0 (mm) defined in Fig. 5.1. From this figure, it is found that the superconductor intensifies the magnetic field at a location of smaller magnetic field. In other words, the depth of ripple between the pole faces is reduced. The numerical results agree with the experimental ones in tendency, although the contribution of the superconductor in the calculation is opposite to that in experiment near the pole face. This could be because the magnetic induction due to the iron core of the magnet actually changes when the superconductor is moved

close to the pole although this effect is neglected in the numerical analysis.

Fig. 5.3 shows the change of ripple value by moving the superconductor close to the pole. Ripple value, δ, is defined as $\delta = (B_{\max} - B_{\min})/(B_{\max} + B_{\min})$. In the experiment, the ripple value was reduced from 1.67 % to 0.76 % at most. Reduction of the ripple in the calculation is much greater than the experiment. This also is ascribed to the above reason why the contribution of the superconductor in the calculation does not agree with experiment near the pole face.

5.3 Numerical analysis

5.3.1 Formulation

In order to compute the magnetic field generated by the high Tc superconductors, the superconducting shielding currents were evaluated based on the current vector potential method(T method) [61,62]. The current vector potential, $\boldsymbol{T}$, is defined as:

$$\nabla \times \boldsymbol{T} = \boldsymbol{J} \quad , \tag{5.1}$$

$$\nabla \cdot \boldsymbol{T} = 0 \qquad \text{(Coulomb gauge)} \quad , \tag{5.2}$$

$$\boldsymbol{n} \times \boldsymbol{T} = 0 \quad \text{(on the surface, } S) \quad , \tag{5.3}$$

where $\boldsymbol{J}$ is the current density and $\boldsymbol{n}$ is the unit normal vector on the surface. The governing equation for the shielding current based on the T method is expressed as follows:

$$\nabla \times \frac{1}{\sigma} \nabla \times \boldsymbol{T} = -\frac{\partial \boldsymbol{B}_o}{\partial t} - \mu_o \frac{\partial \boldsymbol{T}}{\partial t} - \frac{\mu_o}{4\pi} \int \frac{\partial T_n}{\partial t} \nabla \frac{1}{R} dS \quad , \tag{5.4}$$

where σ is the electrical conductivity, $\boldsymbol{B}_o$ is the applied flux density, μ_o is the permeability in vacuum, R is the distance between the source and the field points and T_n is the component of $\boldsymbol{T}$ that is normal to S.

The anisotropy of critical current density, J_c, is taken into consideration. It was reported that the ratio of J_c parallel to the a-b plane of the grain structure to the component

of J_c perpendicular to the a-b plane is about three for the MPMG-YBaCuO superconductors [63]. Hence, the shielding current across the a-b plane can be neglected and the thin plate approximation can be applied. In this approximation it is assumed that the superconductor consists of several thin plates parallel to the a-b plane. This method was verified by the comparison of the experimental and the theoretical electromagnetic forces generated by the MPMG-YBaCuO superconductor [64]. Using the thin approximation, the governing equation can be derived from Eq.(5.4) as:

$$\boldsymbol{n} \cdot \nabla \times \frac{1}{\sigma} \nabla \times (T_n \boldsymbol{n}) = -\boldsymbol{n} \cdot \frac{\partial \boldsymbol{B}_o}{\partial t} - \mu_o \frac{\partial T_n}{\partial t} - \frac{\mu_o}{4\pi} \boldsymbol{n} \cdot \int \frac{\partial T_n}{\partial t} \nabla \frac{1}{R} dS \quad . \tag{5.5}$$

In order to analyze the shielding current field in the superconductor with Eq.(5.5), the critical state model is introduced in the following way. The critical state model describes the mixed state of the type-II superconductors. In this model, it is assumed that the absolute value of the current density is either 0 or the critical current density J_c depending on the induced electrical field, $\boldsymbol{E}$, i.e. [65]:

$$\boldsymbol{J} = J_c \frac{\boldsymbol{E}}{|\boldsymbol{E}|} \qquad \text{if} \quad \boldsymbol{E} \neq 0 \quad , \tag{5.6}$$

$$\frac{\partial \boldsymbol{J}}{\partial t} = 0 \qquad \text{if} \quad \boldsymbol{E} = 0 \quad . \tag{5.7}$$

Describing the dependence of the J_c on the flux density $\boldsymbol{B}$, several models have been proposed, which express J_c as a function of $\boldsymbol{B}$. Among them, the Matsushita model was adopted in our calculation. It is expressed as follows [66]:

$$J_c = \frac{J_{co}}{\sqrt{B}} \quad , \tag{5.8}$$

where J_{co} is the value of J_c when B is 1 T.

Since the $\boldsymbol{J}$-$\boldsymbol{E}$ relation is non-linear, the following iterative calculation scheme is introduced in order to solve Eqs. (5.5), (5.6) and (5.7) consistently.

1. The initial conductivities in all elements are set to be sufficiently large.

2. In the elements where $|\boldsymbol{J}| > J_c$, the conductivities are modified as follows:

$$\sigma^{i+1} = \frac{J_c}{|\boldsymbol{E}^i|} = \frac{J_c}{|\boldsymbol{J}^i|}\sigma^i \tag{5.9}$$

The step 2 is repeated until $|\boldsymbol{J}|$ of all elements become less than J_c.

The magnetic field produced by the TF coils was calculated by using the computer code which was developed by Watanabe [67]. In this code, the finite cross section of the coil is considered instead of using the filament current approximation. The TF coils are composed of two types of elements, arc-shaped elements and pillar-shaped elements. The magnetic field due to each coil element is obtained by the numerical or analytic integration of the Biot-Savart's formulae. The magnetic field calculated by this code is highly accurate.

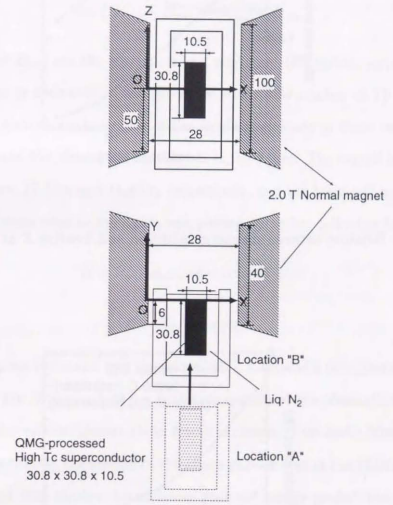

Figure 5.1: Experimental arrangement.

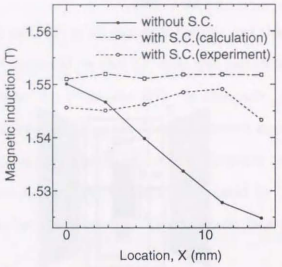

Figure 5.2: Relation between magnetic induction and location X at Y = 9 (mm), Z = 0 (mm).

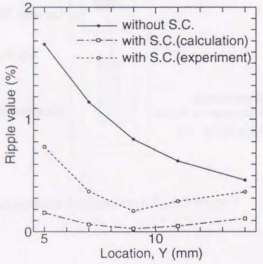

Figure 5.3: Relation between ripple value and location Y.

5.3.2 Feasibility of Ripple Reduction with use of HTSC

Ripple evaluation in the ITER preliminary design

The configuration of the toroidal field magnet system in this study is according to the outline design of ITER [1]. The depth of ripple, δ, is defined as follows:

$$\delta = (B_{max} - B_{min})/(B_{max} + B_{min}) \quad , \tag{5.10}$$

where B_{max} and B_{min} are the maximum and minimum $|\boldsymbol{B}|$ values, respectively. In this study, the ripple is evaluated in the two cases where the number of TF coils, N, are 24 and 20. Fig. 5.4 shows contour lines of the ripple magnitude in these two cases. Shapes of the TF coils and the plasma are also shown in the figure. The overall height and width of the TF coil are 17.32m and 11.45m, respectively, and the total coil current per coil is 9.7 MA. The plasma edge in the figure was plotted using the following formulae:

$$R = R_p + a_p \cos(\theta + \lambda \sin\theta) + \epsilon \quad , \tag{5.11}$$

$$Z = Z_p + a_p \kappa \sin\theta \quad , \tag{5.12}$$

where R_p and a_p are the major and the minor radii, 8.4m and 2.68m, respectively, λ is the triangularity of the D-shape (0.44), κ is the elongation of the plasma(1.7), ϵ and Z_p are the radial and the vertical plasma shifts from the center, 0.1m and 1.90m, respectively.

From the benchmark calculation of the alpha particle loss in the ITER design activity [68], it was found that ripple-induced losses generate highly peaked heat loading at the first wall, while the power loss due to the ripple is not critical for ignition. Therefore, the maximum ripple value in the plasma is required to be less than 2 % in ITER in order to avoid the localized heat load at the first wall.

From Fig.5.4(a), it is seen that the maximum ripple value at the plasma edge is about 1.9 % when N is 24. The required ripple value is satisfied in this case, but the space is not sufficient for the neutral beam injectors between the TF coils. In the case of $N = 20$,

the space for the beams is sufficient. However, the maximum ripple at the plasma edge is about 3.9 % as shown in Fig. 5.4(b), so effort must be made to reduce the magnetic field ripple in this case. The plasma region where the ripple value is more than 2.0 % is localized at the right upper corner of the plasma section. In the following, it is demonstrated that the ripple value of this part in the case of $N = 20$ can be reduced to be less than 2.0 % with use of high Tc superconducting layered plates.

Method of magnetization of high Tc superconductor

The high Tc superconductors are magnetized in the zero-field-cooling process as follows. First, the superconductors are cooled at the location "A"(see Fig. 5.5), where the magnetic field is almost zero. Then, it is moved to the location "B". While approaching to the first wall, the high Tc superconductors start to feel increasing magnetic field. In this way, the high Tc superconductors are magnetized, hence the shielding current is induced in the superconductor. The magnetic field by the TF coils is, thus reformed by the magnetic induction due to the shielding current.

Two arrangements of the superconductors are examined in order to reduce the TF ripple. One is the arrangement in which the superconductors are magnetized by the toroidal component of the field produced by the TF coils. In this case, the superconductors are set in the way where the a-b plane is perpendicular to the toroidal field as shown in Fig. 5.5 (case 1). They are magnetized due to their diamagnetism and reform the magnetic field lines as shown in the figure. The other arrangement is the one in which the superconductors are magnetized through the transverse component of the field. The superconductors are set in the way where the a-b plane is parallel to the toroidal field as shown in Fig. 5.5 (case 2). They also reform the magnetic field lines to reduce the ripple as shown in the figure. We discuss the two cases in light of the ripple reduction.

Reduction of ripple in case 1

The arrangement and geometry of the superconductors are shown in Fig. 5.6. It is a set of MPMG-processed YBaCuO superconductors, which consists of the small superconductor blocks(0.1m × 0.1m × 0.05m). The size of each block is the maximum possible size of MPMG-processed bulk superconductors of single crystal that can be fabricated by using the current technology. The critical current density of each superconductor block, J_{co}, is 3.0×10^8 A/m^2. The assembly of the superconductors is 4.0 m in length and 0.2 m in width and 1.5 m in height. The length of the assembly is chosen so that the superconductors cover the plasma region where the ripple value is more than 2.0 %. Twenty superconductor assemblies are arranged, one located between TF coils. The position of the superconductor assembly is also shown in this figure. It is found that the assemblies do not interfere with neutron beam injectors because the position of the injectors ports is different from that of the assemblies. The superconductors are moved from the location "A" to "B" shown in the figure. The location "B" is 0.5 m away from the edge of the plasma. Figure 5.7 shows the change of the z-component (see Fig. 5.6) of the magnetic field applied to the center of the superconductors when the superconductors are moved from "A" to "B". The applied field increases to 3.15 T. Due to this change of the field, the superconducting currents are induced in the a–b plane, and the TF ripple is consequently reduced.

Figure 5.8 shows the ripple value along the plasma edge for different access distances to the plasma, d. When the distance between the superconductor and the plasma is 0.5 m, the maximum ripple value is reduced to be less than 2 %. From this figure, it is found that the reduction of ripple is strongly affected by the distance between the superconductor and the plasma edge. The possible shortest distance to the plasma edge must be determined with the consideration of the neutron shielding, the working temperature and so on, and it is closely related to the design of the first wall and the blanket structure. This must be considered in the future works. Figure 5.9 shows the relation between the flux density

and the toroidal angle at the maximum ripple location in the case of $d = 0.5$m. The superconductors increase the magnetic field where it is low and decrease the field where it is high, hence the ripple is smoothed and reduced. Figure 5.10 is a contour lines of the ripple magnitude when d is 0.5 m. The ripple value in the whole plasma region is successfully decreased to less than 2 %. Consequently, it is recognized that the presented arrangement is effective to reduce the TF ripple.

Reduction of ripple in case 2

Another arrangement and geometry of the superconductors is shown in Fig. 5.11. Figure 5.12 shows the change of the z-component (see Fig. 5.11) of the magnetic field applied to the superconductors when the superconductors are moved from the location "A" to "C" through "B". In this case, the change of the field is not monotonic, i.e. the field is increased until the location "B", then it starts to decrease. Besides, a magnitude of the change is small compared with that in the case 1.

Figure 5.13 shows the ripple value along the plasma edge for different locations of the superconductors. In the case of $d = 2.0$m, this value corresponds to the location "B" (see Fig. 5.11), the effect of the superconductor is small. Then by moving closer to the plasma, the superconductor increase the maximum ripple value. This is explained as follows. When the superconductors are moved from the location "A" to "B", the applied field is increased, and the shielding current is induced in the a–b plane, leading to the reduction of the ripple. However, the effect of the superconductors is small because the distance, d, is long. When the superconductors are moved close to the plasma furthermore, the applied field is decreased and the opposite shielding current is induced to increase the ripple value.

In this computation, one body superconductors as shown in Fig. 5.11 are considered, although they can not be fabricated by the current technology. It is possible to construct a superconductor assembly which shape is the same as it is shown in Fig. 5.11(b). By

applying this superconductor assembly, the tendency in the change of ripple value is the same like in the case of one body superconductor (see Fig. 5.13), although the magnitude of effect is smaller. Therefore, the configuration shown in Fig. 5.11 can not be applied for the reduction of the reduction of the ripple value.

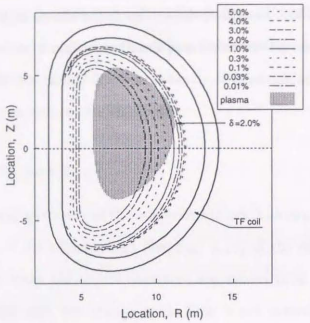

(a) number of TF coils is 24

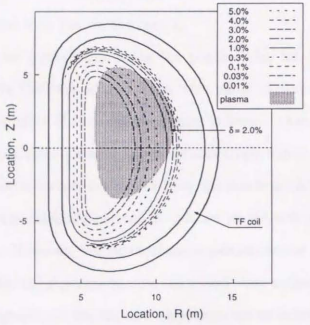

(b) number of TF coils is 20

Figure 5.4: Contour lines of ripple magnitude: (a) number of TF coils is 24, (b) number of TF coils is 20.

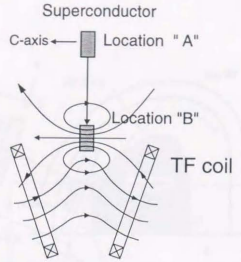

Case 1

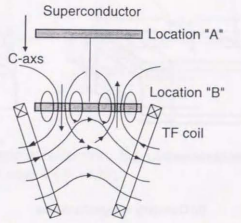

case 2

Figure 5.5: Two arrangements of superconductors between TF coils.

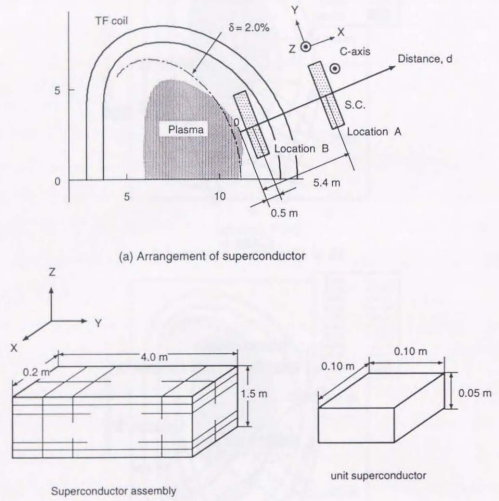

Figure 5.6: Arrangement and geometry of superconductor in case 1.

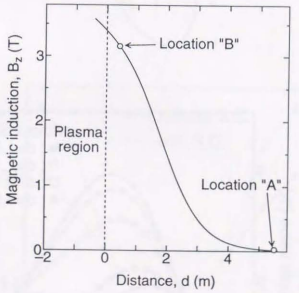

Figure 5.7: Change of magnetic induction, B_z, in the local coordinate in Fig. * at the center of superconductor in case 1 ($N = 20$).

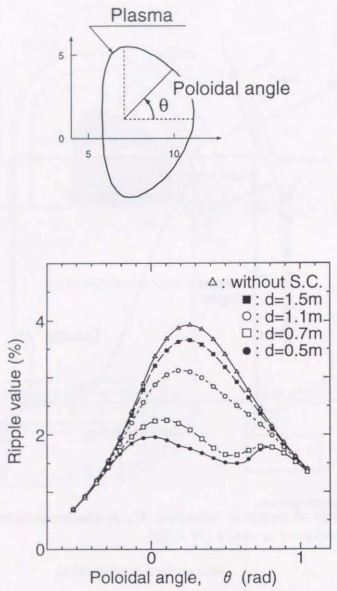

Figure 5.8: Ripple value along plasma edge in different access distances.

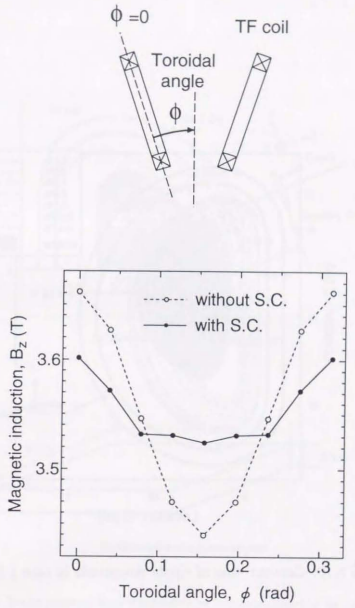

Figure 5.9: Relation between flux density, B_z, in the local coordinate in Fig. 5.6 and toroidal angle at the maximum ripple location ($N = 20$).

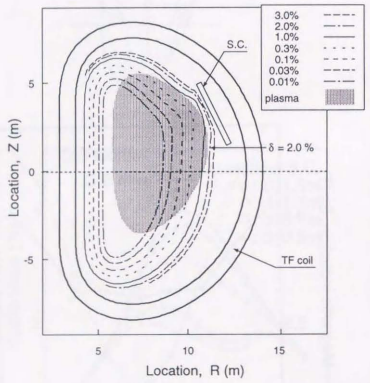

Figure 5.10: Contour lines of ripple magnitude in case 1 ($d = 0.5$m).

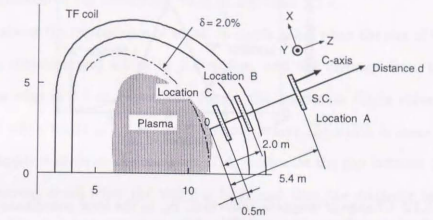

(a) Arrangement of superconductor

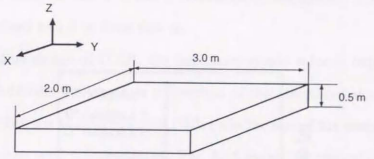

(b) Geometry of superconductor

Figure 5.11: Arrangement and geometry of superconductor in case 2 d ($N = 20$).

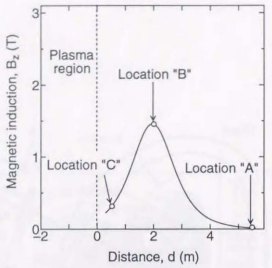

Figure 5.12: Change of magnetic induction, B_z, in the local coordinate in Fig. 5.11 at the center of superconductor in case 2 ($N = 20$).

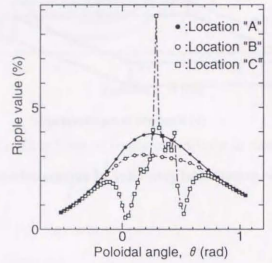

Figure 5.13: Ripple value along plasma edge in different locations ($N = 20$).

5.3.3 Design study

Here, ripple value is evaluated when the length of each side of the superconductor assembly is changed, and a guideline of design of for it is presented. In this parameter survey, the following point was considered as constraint. The superconductor assemblies must not interfere with a neutral beam injectors (NBI). In order to satisfy this requirement, the length in y direction of the assemblies must be less than 3.2 m.

Fig. 5.14 shows the dependence of width on ripple value when the size of the assembly is 0.2 m in x direction and 4.0 m in y direction, and the distance from the assembly to the plasma edge is 0.4 m. From this figure, the maximum ripple value is found to be minimized when width is 1.5 m. In the region where the width is more than 1.5 m, reduction of ripple is small on the contrary. This is because the gap between two adjacent assemblies becomes small when the width is large and then the magnetic induction due to assemblies does not leak out of their gap. This tendency of the width is considered to be same in different size in x and y directions of assemblies. Therefore, the width of assemblies is fixed to 1.5 m from now on.

In the outline design of ITER, the maximum ripple value is required to be less than 2.0 % [1]. In addition the length in y direction of the assemblies must be less than 3.2 m for the assemblies not to interfere with NBI. Here the size of the assemblies which satisfies the above requirements is investigated. Fig. 5.15 shows the critical line for the maximum ripple less than 2.0 % with respect to size in x and y direction. The hatched part in this figure is the region where the superconductor assemblies is realized for ripple reduction in the configuration of ITER.

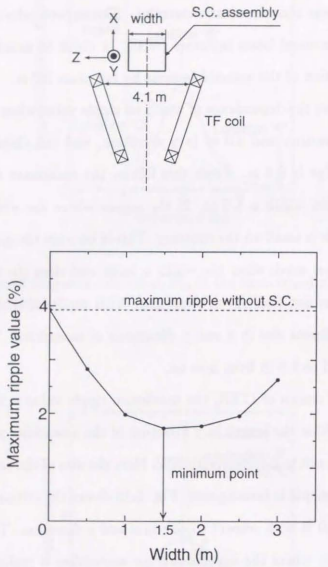

Figure 5.14: Dependence of maximum ripple value in plasma region on width of superconductor assembly (x = 0.2 m, y = 4.0 m, d = 0.4 m).

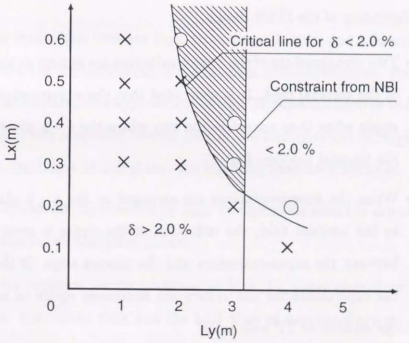

Figure 5.15: Critical line for the maximum ripple less than 2.0 % with respect to size in x and y direction.

5.4 Conclusion

A new method to reduce the TF ripple with use of high Tc superconductors was proposed and quantitatively examined. Conclusions of this chapter are summarized in the following.

(1) The feasibility of ripple reduction through high Tc superconductors is experimentally demonstrated.

(2) The ripple reduction due to high Tc superconductors is numerically estimated in the configuration of the ITER design.

- Two arrangements of the superconductors are aiming at the reduction of ripple of the toroidal field. It is concluded that the superconductors can reduce the ripple when they are set in the way where the a - b plane is perpendicular to the toroidal field(see Fig. 2).
- When the superconductors are arranged as the a - b plane is perpendicular to the toroidal field, the reduction of the ripple is sensitive to the distance between the superconductors and the plasma edge. If the distance is 0.5 m, the superconductor can reduce the maximum ripple to required value, when the number of TF coils is 20.

(3) The parameter survey of size of superconductors is performed, and the guideline of the design of the high Tc superconductor assembly is presented in the configuration of ITER.

Chapter 6

Conclusions

Electromagnetic interaction between high Tc superconductors and tokamak plasmas was examined with the aim of contributing to the progress of fusion research. Based on the elucidation of the interaction, new applications of high Tc superconductors to fusion reactors are proposed and their feasibility was verified in the configuration of large experimental reactor. As the conclusion of this study, the following ones were obtained.

(1) Plasma response in the presence of high Tc superconductors is theoretically examined introducing an simplified model.

- Plasma response in the presence of high Tc superconductors has two time scales: the Alfvén time and the L/R time of superconductors. Owing to the analysis, it was confirmed that unstable plasma can be stabilized with high Tc superconductors in both time scales, which forms a basis for the new application of high Tc superconductors to fusion reactors.
- The characteristic time of plasma stabilization due to high Tc superconductors is estimated considering the hysteresis loss and Joule loss of superconductors.

(2) Based on the above theoretical prediction of electromagnetic interaction between high Tc superconductors and tokamak plasmas, an improvement method for plasma positional instability with use of high Tc superconducting coils was proposed and its feasibility was verified in the configuration of ITER as follows;

- For the accurate estimation of plasma response to high Tc superconducting coils, we developed the code which consistently solves dynamic plasma equilibria and shielding currents in high Tc superconductors.
- Using the developed code, the feasibility of the proposed method is examined in the configuration of ITER design. As a result, it was confirmed that unstable plasma can be stabilized due to high Tc superconducting coils even against the disturbance of $\delta\beta_p = -0.2$ and $\delta li = -0.1$.
- Applicability of high Tc superconductors to fusion reactor environment is verified as follows;
  - Electromagnetic forces on high Tc superconducting coils are calculated and the support structure is considered. A design to accommodate these forces is possible without any difficulty.
  - Nuclear heating due to neutron irradiation was estimated with use of 1-D neutron transport code ANISN. Supposed temperature rise in high Tc superconducting coils is estimated at 0.05 K at the maximum.
  - An experiment with use of high Tc superconductor tapes was carried out to estimate the deterioration of superconductor property due to temperature rise. From the results, it turns out that decrease of stabilizing effect due to supposed temperature rise is negligible.

  It follows from the results that high Tc superconductors provided with the current technology are applicable to the proposed method.

(3) To demonstrate the effect of the method proposed above, conceptual design was performed incorporating the application of high Tc superconductors. Assumptions adopted here is to use the same data base and formula as ITER in principle and not to use any innovative technology other than HTSC stabilizing coils.

- Small ignited tokamak was designed with parameters of moderately lower fusion power of 500 MW, introducing highly elongated plasma stabilized by HTSC stabilizing coils.
- With numerical analysis, it was confirmed that the positional stability is secured with HTSC coils although the elongation of the plasma is set to the high value of 2.3.

(4) A new method to reduce the TF ripple with use of high Tc superconductors was proposed and quantitatively examined.

- The feasibility of ripple reduction through high Tc superconductors was experimentally demonstrated.
- Numerical analysis made it clear that the assembly of the bulk high Tc superconductors can reduce the maximum ripple in plasma to required value in the configuration of ITER.
- The parameter survey of size of superconductors was performed, and the guideline of the design for superconductors was presented in the configuration of ITER.

Bibliography

[1] ITER Joint Central Team, ITER outline design report ITER TAC-4-01(1994)

[2] ITER Joint Central Team, Technical Basis for the ITER Interim Design (1995)

[3] ITER Joint Central Team, ITER Detailed Design Report, Cost Review and Safety analysis (1996)

[4] T.Kato, K.Hayashi, K.Sato, Y.Yaegashi, M.Nagano, T.Ando, T.Isono and H.Tsuji: to be published in Proceedings of ISS'96 (1997)

[5] S.L.Wipf, and H.L.Laquer: Superconducting permanent magnets, IEEE Trans. Magn., Vol.25(1989) 1877–1880

[6] L.Zang, J.Z.Liu and R.N.Shelton: Upper critical field of $(Bi,Pb)_2Sr_2CaCu_2O_8$, Physical Review B, Vol.45 (1992) 4978–4982

[7] K.Watanabe, S.Awaji, H.Yamane, H.Kurosawa, T.Hirai, N.Kobayashi and Y.Muto: Polycrystalline $Y_1Ba_2Cu_3O_7 - \delta$ films prepared by CVD method, Advances in Cryogenic Engineering Vol.38 (1992) 991–996

[8] I.Matsubara, H.Tanigawa, T.Ogura, H.Yamashita, M.Kinoshita and T.Kawai: Uppercritical field and anisotoropy of the high Tc $Bi_2Sr_2Ca_2Cu_3O_x$ phase, Physical Review B, Vol.45 (1992) 7414–7417

[9] J.Shimoyama, N.Tomita, T.Morimoto, H.Kitaguchi, H.Kumakura, K.Togano, H.Maeda, K.Nomura and M.Seido: Jpn. J. Appl. Phys. Vol.31,(1992) L1328–L1338

[10] K.Hayashi: Development of Ag-sheathed Bi2223 superconducting wires and their applications, to be published in Proceedings of ISS'96 (1997)

[11] K.Sato, Physics Wold, Vol.5, No.7, (1992) 37

[12] K.Sato N.Shibuta, H.Mukai, T.Hikata, M.Ueyama, T.Kato and J.Fujikami, Proc. of the 1992 TCSUH Workshop (World Scientific, Singapore, 1992) 349

[13] K.Sato, N.Shibuta, H.Mukai, T.Hikata, M.Ueyama, K.Kato and J.Fujikami, Cryogenics Vol.33 (1993) 243

[14] S.Takamura, H.Sekino, H.Matsushima, M.Kobiyama, T.Hoshiya, K.Sumiya and H.Kuwajima: Magnetization of ceramic Y-Ba-Cu-O and Bi-Sr-Ca-Cu-O after neutron irradiation, Jpn. J. Appl. Phys. Vol.30 (1991) L18–L20

[15] K.Kusagaya, T.Terai, N.Chikumoto, T.Kobayashi, J.Shimoyama and K.Kishio: Neutron fluence dependence of superconducting properties and crystal structure on $Bi_2Sr_2CaCu_2O_y$ single crystal, Physica C, 235-240 (1994) 2975–2976

[16] R. Takahata, H. Ueyama and T. Yotsuya, Elsevier Studies in Appl. Electromagn. in Materials, Vol.1 (1991) 347-350

[17] H. Higasa, M. Shibayama, F. Ishikawa, K. Ono, S. Yokoyama, S. Nakamura, T. Yamada, Y. Yoshida, Trans. IEE, Japan, Vol.113-B, (1993) 768-775

[18] M. Murakami, M.Morita and N.Koyama: Magnetization of $YBa_2Cu_3O_7$ crystal prepared by the quench and melt growth process, Jpn. J. Appl. Phys. Vol.28 (1989)L1125–L1127

[19] M. Murakami, T.Oyama, F.Fujimoto, T.Taguchi, S.Gotoh, Y.Shiohara, N.Koshizuka and S.Tanaka: Large levitation force due to flux pinning in YBaCuO superconductors fabricated by Melt-Powder-Melt-Growth process Jpn. J. Appl. Phys. Vol.29 (1990) L1991–L1994

[20] M. Murakami: Melt processed high-temperature superconductors (World Scientific Publishing Co. Pte. Ltd., 1992)

[21] C.P. Bean: Magnetization of High-Field Superconductors, Rev. Modern Phys., (1964) 31-39

[22] Y.B.Kim, C.F.Hempstead and A.R.Strand: Magnetization and critical supercurrent, Physical review, Vol.129 (1963) 528–535

[23] K.Yasuhochi, T.Ogasawara and N.Usui: Magnetic behavior and effect of transport current on it in superconducting Nb-Zr wire, J. Phys. Soc. Japan, Vol.19 (1964) 1649–1661

[24] D.C.Robinson and A.J.Wootton: An experimental study of tokamak plasmas with vertically elongated cross-section, Nucl. Fusion, Vol.18, (1978)1555–1567

[25] S. Yoshikawa: Application of the Virial theorem to equilibria of toroidal plasmas, Phys. Fluids, Vol.7 (1964) 278–283

[26] S.Seki, H.Momota and R.Itatani: Positional instabilities in a shell-less tokamak, J. Phys. Soc. Japan, Vol.36 (1974)1667–1673

[27] A. Fukuyama, S.Seki, H.Momota and R.Itatani: Positional Instabilities in a tokamak with a resistive shell, Jpn. J. Appl. Phys. Vol.14 (1975)871–877

[28] A.Kameari and S.Niikura: Control of plasma vertical position in tokamak reactors, Nuclear Engineering and Design/Fusion, Vol.2 (1985) 365–373

[29] P.Noll, L.Sonnerup, C.Froger, M.Huguet and J.Last: Forces on the JET vacuum vessel during disruptions and consequent operational limits, Fusion Technology, Vol.15 (1989) 259–266

[30] R.O.Sayer, Y.-K.M.Peng, S.C.Jardin, A.G.Kellman and J.C.Wesley: TSC plasma halo simulation of a DIII-D vertical displacement episode, Nuclear Fusion, Vol. 33 (1993) 969-978

[31] The JET Team: Disruptions and vertical displacement events in JET, Proc. 16th Fusion Energy Conference,(Montreal, 1997) IAEA-CN-64/AP1-18 (1997) 723–730

[32] M.J.Schaffer and B.J.Leikind: Observation of electric currents in diverted tokamak scrape-off layers, Nuclear Fusion, Vol.31 (1991) 1750–1758

[33] S.C.Jardin, N.Pomphrey and J.Delucia: Dynamic modeling of transport and positional control of tokamaks, J. Comput. Phys. Vol.66 (1986) 481–507

[34] E.A.Lazarus et al.: Higher beta at higher elongation in the DIII-D tokamak, Phys. Fluids B, 3, 2220

[35] J.B.Lister et al.: Experimental study of the vertical stability of high decay index plasmas in the DIII-D tokamak, Nuclear Fusion, Vol.30, (1990) 2349

[36] R. Albanese, E. Coccorese, G. Rubinacci: Plasma modeling for the control of vertical instabilities in tokamaks, Nuclear Fusion, Vol.29 (1989) 1013–1023

[37] G.Tinios, S.F.Horne, I.H.Hutchinso, and S.M.Wolfe: Model reduction for axisymmetric tokamak control, Fusion Technology, Vol.24 (1993) 355–365

[38] I.Senda, S.Nishio, T.Tsunematsu, T.Nishino and H.Fujieda: The plasma position control of ITER EDA plasma, Rep. JAERI-Tech 94-018, Japan Atomic Energy Research Institute, Ibaraki-ken (1994)

[39] H.Ninomiya, K.Shinya and A.Kameari: Optimization of currents in field-shaping coils of a non-circular tokamak, Proc. 8th Symp. Eng. Prob. Fusion Res., (1979) 75–80

[40] T.Nishino, K.Shinya, M.Hasegawa and M.Sugihara: User's manual for plasma equilibrium code SYSTEQ, Rep. JAERI-memo 03-141, Japan Atomic Energy Research Institute, Ibaraki-ken (1991)

[41] Y.Yoshida, M.Uesaka and K.Miya: Evaluation of dynamic magnetic force of high Tc superconductor with flux flow and creep, Int. J. Appl. Electromagn. in Mater., Vol.5 (1994) 83–89

[42] Y.Yoshida, M.Uesaka and K.Miya: Magnetic field and force analysis of high Tc superconductor with flux flow and creep, IEEE Trans. Magn., Vol.30 (1994) 3503–3506

[43] H.Hashizume: Magneto-thermo-fluid-mechanical behavior of a first wall of a fusion reactor under off-normal operation, Doctor dissertation, The university of Tokyo (1989)

[44] T.Uchimoto and K.Miya: Design study of high Tc superconducting plasma stabilizer, Proc. 19th Symposium on Fusion Technology, (Lisbon, 1996) 791–794

[45] K. Yamafuji and Y.Mawatari: Electromagnetic properties of high Tc superconductors: relaxation of magnetization, Cryogenics, Vol.32 (1992) 3569–577

[46] S. Kobayashi, T. Kaneko, T. Kato, J. Fujikami and K. Sato: A novel scaling of magnetic field dependencies of critical currents for Ag-sheathed Bi-2223 superconducting tape, Physica C 258 336-340 (1996)

[47] T.Kato, et al.: Current lead using silver-sheathed Bi-based high Tc superconducting tapes, Trans. IEE Japan, Vol.115-A, (1995)251–256 (in Japanese)

[48] W. W. Engle, Jr.: A User's Manual for ANISN, A One-Dimensional Discrete Ordinate Transport Code with Anisotropic Scattering, K-1693, Union Carbide Corporation, Computing Technology Center (1976)

[49] K. Maki, et al. Rep. JAERI-M 91-072 Japan Atomic Energy Research Institute, Ibaraki-ken (1991)

[50] K. Maki, et al. Rep. JAERI-M 91-073 Japan Atomic Energy Research Institute, Ibaraki-ken (1991)

[51] Y.Fujishiro, et al. Cryogenic Engineering Vol.28 No.10 (1993)582-587 (in Japanese)

[52] N.A.Uckan and J.Sheffield: A simple procedure for establishing ignition conditions in tokamaks, Tokamak Start-up, ed. H.Knoepfel (Plenum Press, New York, 1986) 45–72

[53] F.Troyon, R.Gruber, H.Saurenmann, S.Semenzato and S.Succi: MHD-Limits to plasma confinement, Plasma Phys. Control. Fusion, Vol.26 (1984) 209–215

[54] Uckan and ITER Physics Group: ITER physics design guidelines: 1989, ITER Documentation series No. 10, (IAEA, Vienna, 1990)

[55] L.J.Perkins et al.: ITER parametric analysis and operational performance, ITER Documentation series No. 22, (IAEA, Vienna,1991)

[56] D.W.Weissenburger, U.R.Christensen and J.Bialek: The pure tension shape of a thick torus, Rep. PPPL-1353 Princeton Plasma Physics Laboratory, Princeton University, New Jersey (1977) Energy Research Institute, Ibaraki-ken (1991)

[57] W.A.Houlberg, S.E.Attenberger and L.M.Hively: Contour analysis of fusion reactor plasma performance, Nuclear Fusion, Vol.22 (1982) 935–945

[58] S.Ejima, R.W.Callis, J.L.Luxon, R.D.Stambaugh, T.S.Taylor and J.C.Wesley: Volt-second analysis and consumption in Doublet III plasmas, Nuclear Fusion, Vol.22 (1982) 1313–1319

[59] P.N. Yushmanov: Diffusive transport processes caused by ripple in tokamak. Reviews of Plasma Physics, Vol.16 ed. B.B. Kadomtsev (Consultants Bureau, New York, 1990) 117–241

[60] K. Tani, T. Takizuka and M.Azumi: Ripple loss of alpha particles in a tokamak reactor with a non-circular plasma cross-section, Nuclear Fusion, Vol.33 (1993) 903–914

[61] H.Hashizume, T.Sugiura, K.Miya, Y.Ando, S.Akita, S.Torii, Y.Kubota and T.Ogasawara: Numerical analysis of a.c. losses in superconductors, Cryogenics, Vol.31 (1991) 601–606

[62] H.Hashizume, T.Sugiura, K.Miya and S.Toda: Numerical analysis of electromagnetic phenomena in superconductors, IEEE Transactions on Magnetics, Vol.28 (1992)1332–1335

[63] M.Murakami, S.Gotoh, H.Fujimoto, K.Yamaguchi, N.Koshizuka and S. Tanaka: Flux pinning and critical currents in melt processed YBaCuO superconductors, Supercond. Sci. Technol., Vol.4, (1991)S43–S50

[64] M.Uesaka, Y.Yoshida, N.Takeda and K.Miya: Experimental and numerical analysis of three-dimensional high-T_c superconducting levitation systems, Int. J. Appl. Electromagn. in Mater., Vol.4 (1993) 13–25

[65] T.Sugiura, H.Hashizume and K.Miya: Numerical electromagnetic field analysis of type-II superconductors, Int. J. Appl. Electromagn. in Mater., Vol.2 (1991)183–196

[66] T.Matsushita, E.S.Otabe, B.Ni, K.Kimura, M.Morita,M.Tanaka, M.Kimura, K.Miyamoto and K.Sawano: Critical current characteristics in superconducting Y-Ba-Cu-O prepared by the melt process, Jpn. J. Appl. Phys., Vol.30 (1991) L342–L345

[67] T.Watanabe: Highly accurate calculation of magnetic field produced by body current coils of various shapes, Kakuyugokenkyu, Vol. 63 (1990) 482–507 (in Japanese)

[68] K.Tani, T.Takizuka and M.Azumi: Ripple loss of alpha particles in ITER, Rep. JAERI-M 89-086, Japan Atomic Energy Research Institute, Ibaraki-ken (1989)